of CHD. However, it is difficult to understand from MFPs how electrical current abnormalities (such as abnormal current amplitude, direction, and site) occurred in the myocardium.

However, MCG signals are converted into a cardiac electrical image. This image is generally obtained from a two-dimensional (2D) current-arrow map (CAM).[6,14] The CAM gives us a pseudo-2D electrical current distribution consisting of 2D arrows and contours representing the magnitude of arrows. The current distribution parameters (CDPs), which are calculated from the CAM, reflect spatial and time current abnormalities in patients with CHD and other heart diseases.[15–23] However, the criteria and scoring method of the abnormalities using CDPs are still controversial.

Method

Subjects

Table I contains the details of the study population, which consisted of 56 patients (46 males and 10 females) with CHD and 101 normal controls (70 males and 31 females). All of the patients were confirmed to have coronary artery lesions by coronary angiography (CAG). We defined the coronary heart lesions as a vessel diameter >75%. Of the patients, 25 had single-vessel disease (SVD) (right coronary artery disease in six, left anterior descending artery disease in 16, and left circumflex artery disease in three), 13 had double-vessel disease (DVD), and 18 had triple-vessel disease (TVD). Patients who had undergone cardiovascular therapy (coronary artery bypass grafting [CABG], or percutaneous coronary intervention [PCI]) were not included in this study. The normal controls consisted of healthy volunteers with no history of cardiovascular disease and who had a normal ECG at rest (see previous paper[19]). Informed consent was obtained from all subjects.

The members of the control group were selected on the basis of only the ECG results. Therefore, cardiac hypertrophy, dilation, and high blood pressure (HBP), which are measured with other heart functional tests, cannot be excluded in this study. Despite that some cardiac diseases were not completely excluded, we defined a normal control group from the ECG results because an electrophysiological test is used as a first step to diagnose cardiac disease. The CHD group was composed of persons who had coronary artery lesions confirmed by CAG.

MCG System and Data Acquisition

We used a Low-Tc superconducting quantum interference device (SQUID) system with 64 coaxial gradiometers (50-mm baseline and 18-mm diameter) to measure the axial component of the magnetic field (Hitachi High-Technologies Corporation, Tokyo, Japan). The gradiometers were in an 8 × 8 matrix with a pitch of 25 mm, and the measurement area was 175 × 175 mm. Figure 1 illustrates the configuration for the MCG measurement. To adjust the position of the measurement areas for each subject, one gradiometer (position 51) was placed above the position of the xiphoid process. The measured MCG signals at this position

Table I.

Clinical Characteristics of Subjects

	N (n = 101)	CHD (n = 56)
Age (years)	63 + 3	65 + 6
Gender		
Female/Male	31/70	10/46
BMI	23.7	24
HR (bpm)	63	63
Coronary status		
1-vessel		25
LAD		16
LCX		3
RCA		6
2-vessel		13
3-vessel		18

N = normal controls; CHD = patients with coronary heart disease (stenosis > 75%); BMI = body mass index; HR = heart rate; LAD = left anterior descending coronary artery; LCX = left circumflex coronary artery; RCA = right coronary artery.

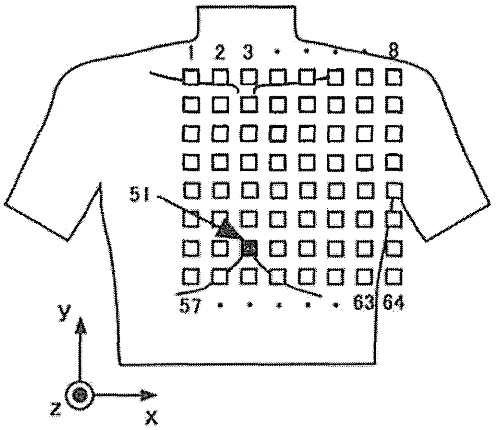

Figure 1. *Configuration for measurement of magnetocardiography (MCG) system (Hitachi High-Technologies Corporation). The 64 SQUID sensors are laid out in an 8 × 8 matrix; the sensor pitch is 25 mm. Channel no. 51 (black square) is placed above the position of the xiphoid process. The MCG system measures the normal component (z-component) of the magnetic field generated by the current in the myocardium.*

were acquired at a sampling rate of 1 kHz and passed through a bandpass (0.1 to 100 Hz) and power line noise filters. The maximum measurement period was 120 seconds, and the MCG signals for all pulses over this period were averaged. A lead II ECG was simultaneously measured as reference signals for MCG averaging.

Spatial and Time Identification of Current Distribution Using MCG

The amplitude and direction of cardiac electrical current vary with the electrical potential difference between normal and ischemic myocardium. To detect these current changes in the myocardium, we calculated CDPs based on maximum current vector (MCV), total current vector (TCV), current integral map (CIM), and current rotation (CR). With the MCV, it is possible to detect local changes in amplitude and direction of the cardiac current.[19] TCV reflects the averaged change in the primary current of the whole heart.[15,16,19] CIM represents the amount of cardiac current during the ventricular depolarization and repolarization phase.[17–19] Furthermore, with the CR, changes in the current distribution pattern can be detected.[21]

Maximum Current Vector

Averaged MCG signals are converted to a CAM. CAM is the method for reconstructing 2D pseudocardiac electrical current vectors at the same number of measurement points. Pseudo current vectors ($I_n = (I_{x,n}, I_{y,n})$) are calculated by taking the derivatives of the normal component ($B_{z,n}$) of the MCG signals at n^th sensor as

$$I_{x,n} = dB_{z,n}/dy \qquad (1)$$

and

$$I_{y,n} = -dB_{z,n}/dx. \qquad (2)$$

CAM can also be calculated by using the tangential components ($B_{y,z}$ and $B_{x,z}$) of the magnetic field instead of $dB_{z,n}/dy$ and $dB_{z,n}/x$ in equations (1) and (2). CAM gives us a spatial electrical activity consisting of 2D arrows ($I_{x,n}$ and $I_{y,n}$) and contours representing the magnitude of the arrows ($I_n = (I_x^2 + I_y^2)^{1/2}$).[14]

To evaluate the spatial current distribution and time variance of current distribution, we calculated the "amplitude ratio (I_{MCV})," "angle (θ_{MCV})," and "angle of difference current vector (φ_{MCV})" of a current arrow with MCV at four time instants (T_1, T_2, T_p, and T_e). The MCV ($I_{max} = (I_{x,max}, I_{y,max})$) indicates a vector with a maximal magnitude of arrows (I_n) at each time instant. Figure 2 schematically shows four time instants (T_1, T_2, T_p, and T_e). Here, T_1 ($T_1 = QRS_{on} + 0.18/\sqrt{(RR)}$) and T_2 ($T_2 = QRS_{on} + 0.20/\sqrt{(RR)}$) are time instants during the ST-T segment. QRS_{on} is the time instant at the beginning of the QRS complex, and RR indicates an averaged R-R interval. The term T_p is the T-wave peak time, and T_e ($T_e = T_p + (T_p - T_2)/2$) indicates time instants during the T-wave peak and the ending of the T wave.

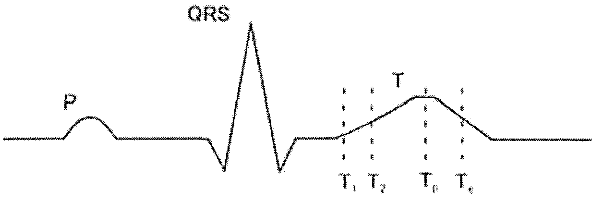

Figure 2. *Schematic representation of four time instants (T_1, T_2, T_p, and T_e) during ventricular repolarization.*

Using CAM at the four time instants, MCV parameters (I_{MCV}, θ_{MCV}, and φ_{MCV}) are calculated from the following equations

(1) I_{MCV}: amplitude ratio

$$\begin{aligned} I_{MCV}(T_2, T_1) &= (I_{max}(T_2) - I_{max}(T_1))/I_{max}(T_1) \\ I_{MCV}(T_p, T_2) &= (I_{max}(T_p) - I_{max}(T_2))/I_{max}(T_2), \\ I_{MCV}(T_p, T_e) &= (I_{max}(T_p) - I_{max}(T_e))/I_{max}(T_e) \end{aligned} \qquad (3)$$

(2) θ_{MCV}: angle

$$\begin{aligned} \theta_{MCV}(T_1) &= \tan^{-1}(I_{y,max}(T_1)/I_{x,max}(T_1)) \\ \theta_{MCV}(T_2) &= \tan^{-1}(I_{y,max}(T_2)/I_{x,max}(T_2)) \\ \theta_{MCV}(T_p) &= \tan^{-1}(I_{y,max}(T_{max})/I_{x,max}(T_p))' \\ \theta_{MCV}(T_e) &= \tan^{-1}(I_{y,max}(T_e)/I_{x,max}(T_e)) \end{aligned} \qquad (4)$$

(3) φ_{MCV}: angle of difference current vector

$$\begin{aligned} \varphi_{MCV}(T_2, T_1) &= \tan^{-1}((I_{y,max}(T_2) - I_{y,max}(T_1)) \\ &\quad /(I_{x,max}(T_2) - I_{x,max}(T_1)) \\ \varphi_{MCV}(T_p, T_2) &= \tan^{-1}((I_{y,max}(T_p) - I_{y,max}(T_2)) \\ &\quad /(I_{x,max}(T_p) - I_{x,max}(T_2)), \\ \varphi_{MCV}(T_p, T_e) &= \tan^{-1}((I_{y,max}(T_p) - I_{y,max}(T_e)) \\ &\quad /(I_{x,max}(T_p) - I_{x,max}(T_2)) \end{aligned} \qquad (5)$$

where the angles (θ_{MCV} and φ_{MCV}) are defined as in Figure 3A and B. Amplitude ratio (I_{MCV}) and angle of difference current vector (φ_{MCV}) were calculated from nearby time points (T_2 and T_1, T_p and T_2, T_p and T_e). Current amplitude and current angle during the ventricular repolarization phase slowly and continuously change for healthy subjects.[24] Therefore, we consider that such changes at nearby time points are proper parameters for detecting abnormalities in the ventricular repolarization phase.

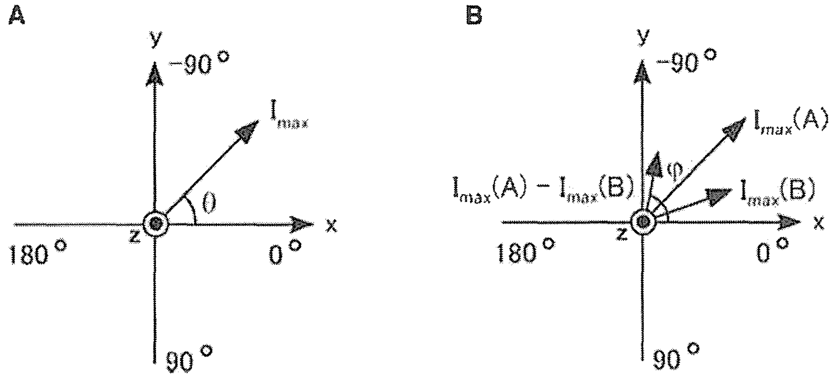

Figure 3. *Definition of current angle (range: +0 to +180 degrees and −0 to −180 degrees). (A) Definition of angle of maximal current vector (MCV). I_{max} indicates maximal current vectors. (B) Definition of angle of difference current vector. I_{max} (A) and I_{max} (B) indicate maximal current vectors at time instants A and B, respectively. I_{max} (A) − I_{max} (B) show the difference current vector.*

Total Current Vector

The TCV based on the CAM is reflected simply to the electrical axis of the heart.[15,16] TCV ($\mathbf{I}_{TCV} = (I_x, I_y)$) is calculated as a vector value by using current vector ($\mathbf{I}_n$) at each sensor,

$$\mathbf{I}_{TCV} = \sum_{n=1}^{64} \mathbf{I}_n(T), \qquad (6)$$

where T indicates the calculated time. We calculated the "amplitude ratio (I_{TCV})," "angle (θ_{TCV})," and "angle of difference current vector (φ_{TCV})" of TCV at four time instants (T_1, T_2, T_p, and T_e) as a spatial-time current parameter. Then, TCV parameters (I_{TCV}, θ_{TCV}, and φ_{TCV}) are calculated in order to substitute TCV vectors (I_x, I_y, and I_{TCV}) for current vectors ($I_{x,max}$, $I_{y,max}$, and I_{max}) in Equations (3)–(5). The definitions of θ_{TCV} and φ_{TCV} are the same as that for the MCV angle (Fig. 2).

Current Integral Map

The CIM is a method of heart disease analysis based on CAM.[17–19] This map represents the amount of current during ventricular depolarization and repolarization. CIM is obtained through the summation of amplitude of current arrows (I_n) during ventricular depolarization and repolarization phases. CIM consists of two parameters ($JTi/QRSi_{max}$ and $JTi/QRSi_{sum}$). The $JTi/QRSi_{max}$ parameter is the ratio of the maximum integral values during ventricular depolarization and repolarization phases, and $JTi/QRSi_{sum}$ is the ratio of the summed current integral values for all channels during ventricular depolarization and repolarization phases.

Current Rotation

CR represents the degree of rotation of the 2D current vector.[21] This value can quantify change in a current distribution pattern. The CR value (I_{rot}) at the nth measurement point is calculated from the following equation (see Fig. 4)

$$\mathrm{Irot}_n = \frac{I_{y,n+1} - I_{x,n-8} - I_{y,n-1} + I_{x,n+8}}{I_{n,max}}, \qquad (7)$$

where $I_{n,max}$ denotes the maximal amplitude of CAM for all sensors. CR parameters consist of maximal (Irot_{max}) and minimal (Irot_{min}) values of Irot_n at time instant T_p, and the difference value (dIrot) between maximal (Irot_{max}) and minimal (Irot_{min}) values of Irot_n.

Statistical Analysis of MCG Parameters

To verify whether it was possible to discriminate between patients with CHD from normal controls using the 25 MCG parameters (MCV, TCV,

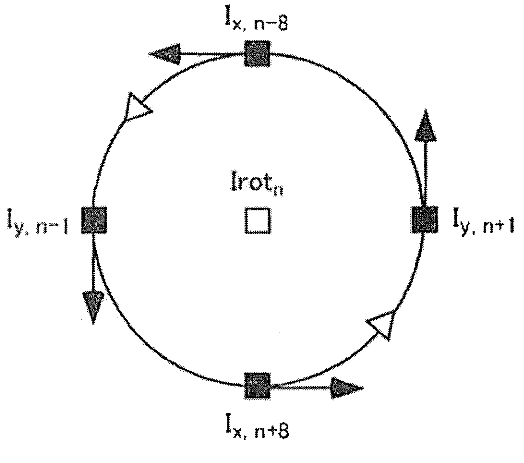

Figure 4. *Rotation direction for summation ($\mathrm{Irot}_n = I_{y,n+1} - I_{x,n-8} - I_{y,n-1} + I_{x,n+8}$).*

CIR, and CR), we calculated the area under the receiver operating characteristic (ROC) curve (A_z value).[25] The ROC curve is an index of diagnostic accuracy, and a ROC graph is a plot of all of the sensitivity/specificity pairs resulting from continuously varying the decision threshold for MCG parameters. Here, we use four MCG parameters with a high A_z value ($A_z \geq 0.75$) to detect patients with CHD.

Detection Criterion for CHD Using MCG Parameters

In the MCG test to detect CHD patients, normal ranges of four MCG parameters were determined by an optimal decision threshold that gave the maximum value of the sum of sensitivity and specificity. Furthermore, each MCG parameter was assigned a score of "0" or "1" based on the normal range for an individual subject. Then, the total score of four MCG parameters was calculated. This total score was in the range from "0" to "4." Based on the assumption that a subject with a total score over "1" was strongly suspected of having CHD, we were able to distinguish electrical current abnormalities in CHD patients. We call this total score the repolarization abnormal score. To evaluate the effectiveness of this criterion, the sensitivity and specificity of the MCG test were calculated.

Results

Evaluation of MCG Parameters Based on Current Distributions

Table II lists the A_z values of all MCG parameters. MCG parameters with a high A_z value ($A_z \geq 0.75$) are marked with an asterisk (*). As indicated in the table, seven MCG parameters had a high A_z value.

Maximum Current Vector

MCV angles had high A_z values. In particular, the MCV angle at the T-wave peak (θ_{MCV} (T_p)) had the maximum A_z value (0.808) of all MCV parameters. The angle of difference current vector (φ_{MCV} (T_p, T_2) and φ_{MCV} (T_p, T_e)) also had high A_z values (0.755 and 0.780). On the contrary, the A_z values of MCV amplitude were low (0.572–0.704).

Total Current Vector

The A_z value of the TCV angle at the T-wave peak (θ_{TCV} (T_p)) was 0.832, the maximum A_z value of all MCG parameters. Furthermore, the angle of difference current vector (φ_{TCV} (T_p, T_2) and φ_{TCV} (T_p, T_e)) also had high A_z values (0.801 and 0.792). These A_z values of TCV angle and angular difference were notably higher than those of MCV. However, as in the case of MCV, the A_z values of the amplitude during the ventricular depolarization phase were low (0.534–0.697).

Table II.

MCG Parameters and Their A_z Values. The 25 MCG Parameters Are Categorized as MCV, TCV, CIM, and CR

Parameter Group	Name	Unit	A_z
MCV			
Amplitude	I_{MCV} (T_2, T_1)	–	0.572
	I_{MCV} (T_p, T_2)	–	0.704
	I_{MCV} (T_p, T_e)	–	0.594
Angle	θ_{MCV} (T_1)	degree	0.613
	θ_{MCV} (T_2)	degree	0.643
	θ_{MCV} (T_p)	degree	0.808*
	θ_{MCV} (T_e)	degree	0.743
Angle of difference current vector	φ_{MCV} (T_2, T_1)	degree	0.689
	φ_{MCV} (T_p, T_2)	degree	0.755*
	φ_{MCV} (T_p, T_e)	degree	0.780*
TCV			
Amplitude	I_{TCV} (T_2, T_1)	–	0.644
	I_{TCV} (T_p, T_2)	–	0.697
	I_{TCV} (T_p, T_e)	–	0.534
Angle	θ_{TCV} (T_1)	degree	0.689
	θ_{TCV} (T_2)	degree	0.681
	θ_{TCV} (T_p)	degree	0.832*
	θ_{TCV} (T_e)	degree	0.760*
Angle of difference current vector	φ_{TCV} (T_2, T_1)	degree	0.708
	φ_{TCV} (T_p, T_2)	degree	0.801*
	φ_{TCV} (T_p, T_e)	degree	0.792*
CIM	$JTi_{max}/QRSi_{max}$	–	0.641
	$JTi_{sum}/QRSi_{sum}$	–	0.646
CR	$Irot_{max}$	–	0.607
	$Irot_{min}$	–	0.673
	dI_{rot}	–	0.661

*$A_z > 0.75$

A_z = area under the ROC curve; ROC curve = receiver operating characteristic curve; MCV = maximal current vector; TCV = total current vector; CIM = current integral map; CR = current rotation

Current Integral Map and Current Rotation

The A_z values of maximum and summation integral values ($JTi_{max}/QRSi_{max}$ and $JTi_{sum}/QRSi_{sum}$) were higher than 0.60, and there was not much difference between $JTi_{max}/QRSi_{max}$ and $JTi_{sum}/QRSi_{sum}$. In contrast, CR parameters ($Irot_{max}$ (T_p), $Irot_{min}$ (T_p), and dIrot (T_p)), had low A_z values (0.607–0.673).

These results indicate that current angles (MCV and TCV angles) at the T-wave peak were most effective for distinguishing electrical current abnormalities in CHD patients. Furthermore, angle of difference current vector (MCV and TCV) during the ST-T segment also had high detection accuracy for patients with CHD.

Table III.

Normal Ranges of Four MCG parameters (θ_{MCV} (T_p), θ_{TCV} (T_p), θ_{TCV} (T_p-T_2), and θ_{TCV} (T_p-T_e))

Parameter Name	Unit	Normal Range
θ_{MCV} (T_p)	degree	$6^\circ < \theta_{MCV} (T_p) < 88^\circ$
θ_{TCV} (T_p)	degree	$16^\circ < \theta_{TCV} (T_p) < 69^\circ$
φ_{TCV} ($T_p > T_2$)	degree	$27^\circ < \varphi_{TCV} (T_p, T_2) < 59^\circ$
φ_{TCV} ($T_p > T_e$)	degree	$2^\circ < \varphi_{TCV} (T_p, T_e) < 82^\circ$

Detection of Electrical Current Abnormalities in CHD Patients Using MCG Parameters

Criteria

To detect the electrical current abnormalities in CHD patients, we used four MCG parameters (θ_{MCV} (T_p), θ_{TCV} (T_p), (φ_{TCV} (T_p, T_2), and (φ_{TCV} (T_p, T_e)) with high A_z values. Table III presents the normal ranges of four MCG parameters, which were determined by an optimal decision threshold. This threshold gave the maximum values of the sum of sensitivity and specificity obtained from the ROC curve (see Fig. 5). The ROC curve of θ_{TCV} (T_p) is plotted in Figure 5.

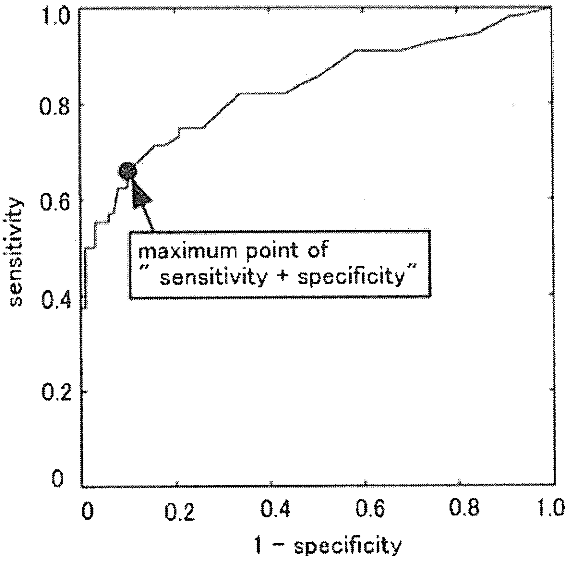

Figure 5. *Receiver operating characteristic curve of total current vector (TCV) angle (θ_{TCV} (T_p)). The black circle shows the maximum point of the sum of sensitivity and specificity.*

Scoring

Figure 6 illustrates the percentage distributions of subjects—both normal controls (left) and CHD patients (right)—with each repolarization abnormal score ("0" to "4") of the four MCG parameters. We see from Figure 5 that the percentage of normal subjects with a repolarization abnormal score of "0" was 74.3%. In contrast, the percentage of CHD patients with a repolarization abnormal score of "0" was about 15%. Therefore, based on the assumption that a subject with a repolarization abnormal score over "1" is strongly suspected of having CHD, the sensitivity and specificity of the MCG test were 85.7% and 74.3%, respectively.

Figure 7 shows the averaged repolarization abnormal score for normal controls and for patients with SVD, DVD, and TVD. The averaged repolarization abnormal score for normal controls was the lowest ("0.53"). On the other hand, the averaged repolarization abnormal score for patients with TVD was "2.67." This score was high compared to the averaged repolarization abnormal score for patients with SVD and DVD.

Discussion

High Accuracy for Detection of CHD Using MCV and TCV

MCV and TCV angles during the ST-T segment had high A_z values. In myocardial ischemia and infarction, the action potential at the site of a lesion changes significantly. For example, it may disappear or exhibit prolonged ventricular repolarization and prolonged discharge intervals.[26,27] These abnormal action potentials in the ischemic myocardium change the direction of cardiac electrical current. Therefore, it is highly possible that MCV and TCV angles could be used to detect spatial current abnormalities in myocardial ischemia and infarction.

However, angle of difference current vector (MCV and TCV) during ventricular repolarization also resulted in high detection accuracy for CHD patients. In ECG studies, abnormal T waves (tall, flattened, inverted, and biphasic) are caused by myocardial ischemia and infarction influences.[28] These abnormal T waves indicate that the direction of electrical current in the ischemic myocardium changes temporally. Therefore, it is conceivable that the angle of difference current vector reflect time-sequential changes due to current direction dispersion in ischemic myocardium.

In the statistical analysis of CDPs (see Table II), each A_z value of TCV angle and angle of difference current vector were notably higher than that of MCV. In a previous study, the TCV angle during the ventricular repolarization phase was stable with low standard deviation in the case of all age groups that were evaluated.[22] Furthermore, it is noted that with TCV it is possible to detect very low electrical current in a fetal heart.[16] It can, therefore, be concluded that TCV is a useful

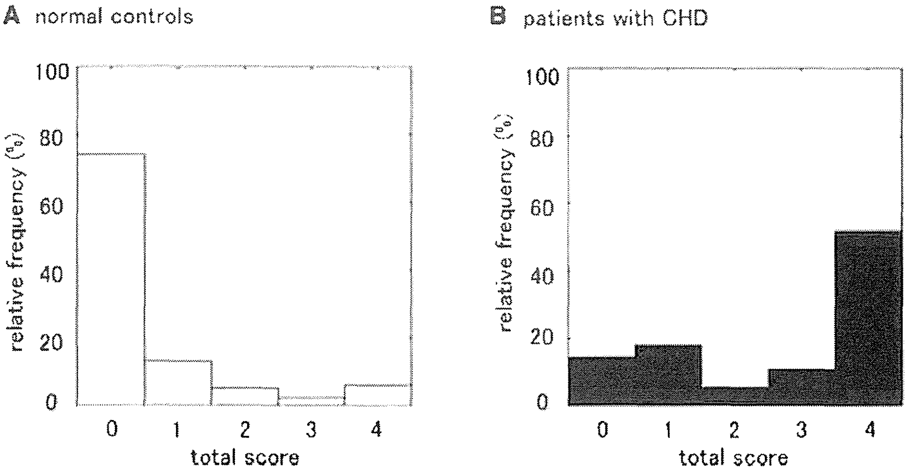

Figure 6. *Percentage distributions of the number of subjects with each repolarization abnormal score (white bars: normal controls, black bars: coronary heart disease patients).*

parameter that is less affected by individual variables such as age and amplitude of cardiac current.

As can be seen, TCV angle and angle of difference current vector difference could accurately detect patients with coronary heart lesions with a vessel diameter over 75%. Therefore, it might be able to detect coronary stenoses of less than 50% diameter, which are clinically significant, in the same way.

Comparison between CDPs and MFPs

Some clinical studies based on MFPs for detection of CHD have been done. Table IV lists the sensitivities and specificities of three MCG tests using MFPs and CDPs.

Park et al. examined four MFPs (method I) taken from the MCG signals during the ventricular repolarization phase for 185 patients with ischemic syndrome.[12] In their study, sensitivity and specificity for the patients were 86.4% and 82.5% using automatic diagnosis. We applied method I for our data listed in Table I. Consequently, sensitivity had a similar value (85.7%), but specificity had a lower value (64.4%). Tolstrup et al. investigated seven MFPs (method II) during ventricular repolarization obtained from 125 patients experiencing chest pain.[13] The sensitivity and specificity of seven MFPs were 76.4% and 74.3%. Hailer et al. examined the semiautomated classification system (method III), which is based on the dipolar structure of current density vector (CDV) map and the direction of the main CDVs, for patients with coronary artery disease patients.[29,30] The calculation of 2D CDV map is based on the inverse problem solution. Sensitivity and specificity for the patients were 73.3% and 70.1%. On the other hand, sensitivity and specificity of the MCG test done using our CDPs were 85.7% and 74.3%. Although each study used different criteria and subjects, these results indicate that the CDPs and MFPs had a similar sensitivity and specificity range from 70% to 85%.

Using the normal ranges of four CDPs established from normal MCG, we obtained a high sensitivity (85.7%) in the CHD patients. Furthermore, the average repolarization abnormal score of four CDPs in the CHD group with severe TVD was higher (2.67) than in the other groups (normal control: 0.53). There is a strong possibility that the repolarization abnormal score correlated with the number of major stenotic vessels. This result indicates the scoring method using four CDPs reflected the electrical activation dispersion due to ischemia and ischemic (infarct) area. It was concluded that CDPs may help to diagnose spatial-time current abnormalities in the myocardium during ventricular repolarization.

Table IV.

Sensitivity and Specificity of MCG Test for Detection of CHD

	Sensitivity	Specificity
Current distribution parameters (CDPs)		
Our result	85.7%	74.3%
Method III[30]	73.3%	70.1%
Magnetic field parameters (MFPs)		
Method I[12]	86.4% (85.7%*)	82.5% (64.4%*)
Method II[13]	76.4%	74.3%

*Sensitivity and specificity of Method I were applied for our data listed in Table I.

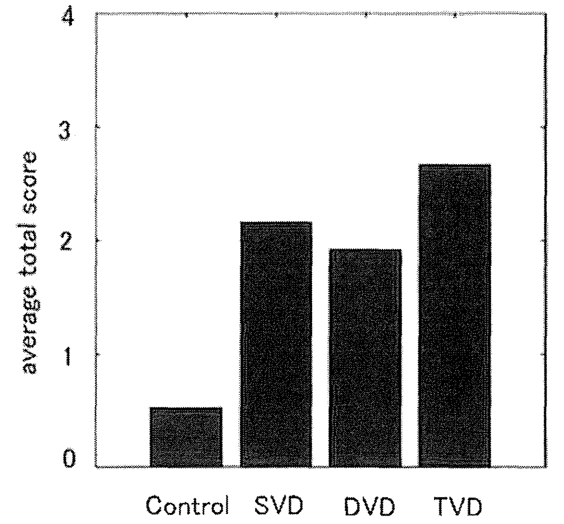

Figure 7. *Averaged repolarization abnormal score of normal controls and patients with single-vessel disease, double-vessel disease, and triple-vessel disease TVD.*

To verify that the CDPs reflect ischemic and infarction size, we calculated the correlations between four CDPs (θ_{MCV} (T_p), θ_{TCV} (T_p), φ_{TCV} (T_p, T_2), and φ_{TCV} (T_p, T_e)) and left ventricular ejection fraction (LVEF). LVEF is an important marker of the left ventricular dysfunction and reflects ischemic and infarct size. Figure 8A–D shows the scatter plots of LVEFs against the four CDPs (θ_{MCV} (T_p), θ_{TCV} (T_p), φ_{TCV} (T_p, T_2), and φ_{TCV} (T_p, T_e)) for 16 patients with CHD. Here, we normalized each CDP by using their median value for healthy volunteers. Figure 8A–D also shows the fitted regression lines calculated for the scatter plots. Average LVEF was 55 ± 14% and ranged from 34% to 75% in the 16 patients. The correlation coefficients between the LVEF and four CDPs were less than −0.35. In particular, φ_{TCV} (T_p, T_e) had the highest correlation ($r = -0.59$). This result might indicate that the level of repolarization current abnormality is associated with ischemic left ventricular dysfunction due to ischemia.

Study Limitations

We should point out several limitations in this study. First, the control group was identified from only the ECG results. Therefore, cardiac hypertrophy, dilation, and HBP, which are detected by other heart functional tests, cannot be excluded in this study. Second, it is not enough to compare the results gotten from the MCG parameters with other heart function parameters (BP, ejection fraction, and ST elevation). In particular, we need to investigate whether abnormal CDPs in

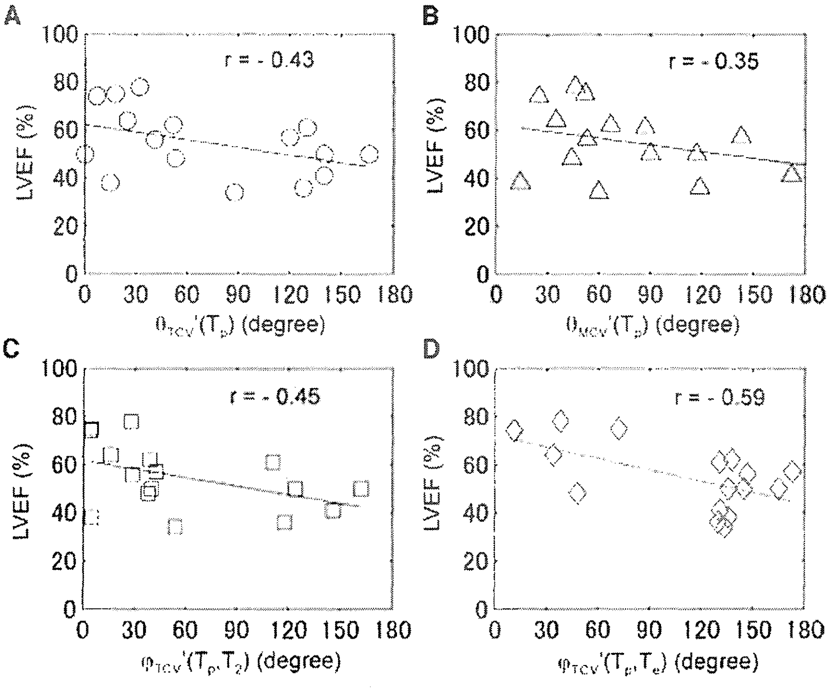

Figure 8. *Scatter plots of left ventricular ejection fractions against the four current distribution parameters (CDPs). (A) θ_{MCV} (T_p), (B) θ_{TCV} (T_p), (C) φ_{TCV} (T_p, T_2), and (D) φ_{TCV} (T_p, T_e)). We normalized each CDP by using their median value for healthy volunteers.*

CHD patients result from CHD or high BP, since half of CHD patients generally had HBP. Third, we defined the coronary heart lesions as a vessel diameter over 75%. Fourth, the number of patients with CHD (56 patients) was small.

Despite these limitations, the repolarization abnormal score and criteria using four CDPs in CHD patients can reflect lesion size and time changes of electrical activation dispersion due to ischemia.

Future Work

To evaluate the improvement in cardiac function, we will compare the CDPs of CHD patients before and after coronary revascularization. We also consider it important to distinguish abnormalities in ventricular repolarization for CHD patients with diabetes, hypertension, hypertrophy, and rhythm conductance abnormalities by using CDP.

Acknowledgments: We gratefully thank Noriko Takuma, Nobuo Sasaki of Hitachi General Hospital, Satsuki Yamada of Mayo Clinic, and Keiji Tsukada of Okayama University for their valuable advice. Furthermore, we are also grateful to Shigeaki Naito, Toru Okihara, Hiroki Ihara, Hiroyuki Suzuki, and Masahiro Murakami of Hitachi-High Technologies Corporation for planning the MCG measurements.

References

1. Mackay J, Mensah G. Atlas of heart disease and stroke. Geneva: World Health Organization, 2004.
2. Ikeda K, Kamimura H. Studies on characteristics of cause of death in Japan. Tokyo Metropolitan Research Laboratory of Public Health Annual Reports 1998; 41:1–4.
3. Fortuin NJ, Weiss JL. Exercise stress testing. Circulation 1977; 56:699–712.
4. Polizos G, Ghamsary M, Ellestad MH. The severity of myocardial ischemia can be predicted by the exercise electrocardiogram. Cardiology 2005; 104:215–220.
5. Gianrossi R, Detrano R, Mulvihill D, Lehmann K, Dubach P, Colombo A, McArthur D, et al. Exercise-induced ST depression in the diagnosis of coronary artery disease. A meta-data. Circulation 1989; 80:87–98.
6. Cohen D, Lepeschkin E, Hosaka H, Massell BF, Myers G. Abnormal patterns and physiological variations in magnetocardiograms. J Electrocardiol 1976; 9:398–409.
7. Hoeing HE, Daalmans GM, Bar L, Bommel F, Paulus A, Uhl D, Weisse HJ, et al. Multi channel DC SQUID sensor array for biomagnetic applications. IEEE Trans Magn 1991; 27:2777–2785.
8. Drung D, Koch H. An electrical second-order gradiometer for biomagnetic applications in clinical shielded rooms. IEEE Trans Appl Supercond 1993; 3:2594–2597.
9. Tsukada K, Haruta Y, Adachi A, Ogata H, Komuro T, Ito T, Takada Y, et al. Multichannel SQUID system detecting tangential components of the cardiac magnetic field. Rev Sci Instrum 1995; 66:5085–5091.
10. Tsukada K, Kandori A, Miyashita T, Sasabuchi H, Suzuki H, Kondo S, Komiyama Y, et al. A simplified superconducting quantum interference device system to analyze vector components of a cardiac magnetic field. Proc 20th Int Conf IEEE/EMBS 1998; 524–527.
11. Seki Y, Kandori A, Suzuki D, Ohnuma M. Open-type magnetocardiograph with cylindrical magnetic shield. Appl Phys Lett 2005; 86:243902.
12. Park JW, Jung F. Qualitative and quantitative description of myocardial ischemia by means of magnetocardiography. Biomed Technik 2004; 49:267–273.
13. Tolstrup K, Madsen BE, Ruiz JA, Greenwood SD, Camacho J, Siegel RJ, Gertzen HC. Non-invasive resting magnetocardiographic imaging for the rapid detection of ischemia in subjects presenting with chest pain. Cardiology 2006; 106:270–276.
14. Miyashita T, Kandori A, Tsukada K, Sato M, Terada Y, Horigome H, Mitsui. Construction of tangential vectors from normal cardiac magnetic field components. Proc 20th Int Conf IEEE/EMBS 1998; 520–523.
15. Kandori A. Kanzaki H. Miyatake K, Hashimoto S, Ito S, Tanaka N, Miyashita, et al. A method for detecting myocardial abnormality by using a total current-vector calculated from ST-segment deviation of a magnetocardiogram signal. Med Biol Eng Comput 2001; 39: 21–28.
16. Kandori A, Miyashita T, Tsukada K, Hosono T, Miyashita S, Chiba Y, Horigome H, et al. Prenatal diagnosis of QT prolongation by fetal magnetocardiogram-use of QRS and T-wave current-arrow maps. Physiol Meas 2001; 22:377–387.
17. Tsukada K, Miyashita T, Kandori A, Mitsui T, Terada Y, Sato M, Shiono J, et al. An iso-integral technique using magnetocardiogram, and its possible use for diagnosis of ischemic heart disease. Int J Cardiac Imaging 2000; 16:55–66.
18. Shiono J, Horigome H, Matsui A, Terada Y, Watanabe S, Miyashita T, Tsukada K. Evaluation of myocardial ischemia in Kawasaki disease using an isointegral map on magnetocardiogram. Pacing Clin Electrophysiol 2002; 25:915–921.
19. Yamada S, Yamaguchi I. Magnetocardiograms in clinical medicine: Unique information on cardiac ischemia, arrhythmias, and fetal diagnosis. Intern Med 2005; 44:1–19.
20. Kandori A, Kanzaki H, Miyatake K, Hashimoto S, Ito S, Tanaka N, Miyashita T, et al. A method for detecting myocardial abnormality by using a current-ratio map calculated from an exercise-induced magnetocardiogram. Med Biol Eng Comput 2001; 39: 29–34.
21. Kanzaki H, Nakatani S, Kandori A, Tsukada K, Miyatake K. A new screening method to diagnose coronary artery disease using multichannel magnetocardiogram and simple exercise. Basic Res Cardiol 2003; 98:124–132.
22. Kandori A, Ogata K, Watanabe Y, Takuma N, Tanaka K, Murakami M, Miyashita T, et al. Space-time database for standardization of adult magnetocardiogram—making basic MCG standard parameters. Pacing Clin Electrophysiol (to be published).
23. Kandori A, Oe H, Miyashita K, Miyashita T, Ohira S, Naritomi H. Chiba Y, et al. Magneto-encephalographic measurement of neural activity during period of vertigo induced by cold caloric stimulation. Neueroscì Res 2003; 46: 281–288.
24. Miyashita T, Kandori A, Tsukada K, Yamada S, Shiono J, Horigome H, Terada Y, et al. Multiple-current-vector diagrams for evaluating inhomogeneity of myocardial activity – applied to ischemic heart disease and cardiomyopathy. Proc 13th Int Conf BIOMAG 2002; 582–583.
25. Zweig MH, Campbell G. Receiver-operating characteristic (ROC) plots: A fundamental evaluation tool in clinical medicine. Clin Chem 1993; 39:561–577.
26. Cinca J, Janse MJ, Morena H, Candell J, Valle V, Durrer D. Mechanism and time course of the early electrical changes during acute coronary artery occlusion. An attempt to correlate the early ECG changes in man to the cellular electrophysiology in the pig. Chest 1980; 77:499–505.
27. Downar R, Janse MJ, Durrer D. The effect of acute coronary occlusion on subepicardial transmembrane potentials in the intact porcine heart. Circulation 1977; 56:217–224.
28. Channer K, Morris F. ABC of clinical electrocardiography: Myocardial ischemia. BMJ 2002; 324:1023–1026.
29. Hailer B, Chaikovsky I, Auth-Eisernitz S, Schäfer H, Steinberg F, Grönemeyer DH. Magnetocardiography in coronary artery disease with a new system in an unshielded setting. Clin Cardiol 2003; 26:465–471.
30. Hailer B, Chaikovsky I, Auth-Eisernitz S, van Leeuwen P. The value of magnetocardiography in patients with and without relevant stenoses of the coronary arteries using an unshielded system. Pacing Clin Electrophysiol 2005; 28:8–16.

RESEARCH ARTICLE

Human Mutation

OFFICIAL JOURNAL

HGVS
HUMAN GENOME
VARIATION SOCIETY
www.hgvs.org

Novel KCNE3 Mutation Reduces Repolarizing Potassium Current and Associated With Long QT Syndrome

Seiko Ohno,[1] Futoshi Toyoda,[2] Dimitar P Zankov,[2,3] Hidetada Yoshida,[1] Takeru Makiyama,[1] Keiko Tsuji,[3] Toshihiro Honda,[4] Kazuhiko Obayashi,[5] Hisao Ueyama,[6] Wataru Shimizu,[7] Yoshihiro Miyamoto,[8] Shiro Kamakura,[7] Hiroshi Matsuura,[2] Toru Kita,[1] and Minoru Horie[3]*

[1]*Department of Cardiovascular Medicine, Kyoto University Graduate School of Medicine, Kyoto, Japan*

[2]*Department of Physiology, Shiga University of Medical Science, Shiga, Japan*

[3]*Department of Cardiovascular and Respiratory Medicine, Shiga University of Medical Science, Shiga, Japan*

[4]*Cardiovascular Center, Saiseikai Kumamoto Hospital, Kumamoto, Japan*

[5]*Obayashi Clinic, Kyoto, Japan*

[6]*Department of Molecular Medical Biochemistry, Shiga University of Medical Science, Shiga, Japan*

[7]*Division of Cardiology, Department of Internal Medicine, National Cardiovascular Center, Osaka, Japan*

[8]*Laboratory of Molecular Genetics, National Cardiovascular Center, Osaka, Japan*

Communicated by Claude Férec

Received 25 January 2008; accepted revised manuscript 5 May 2008.

Published online 20 March 2009 in Wiley InterScience (www.interscience.wiley.com). DOI 10.1002/humu.20834

ABSTRACT: Long QT syndrome (LQTS) is an inherited disease involving mutations in the genes encoding a number of cardiac ion channels and a membrane adaptor protein. Among the genes that are responsible for LQTS, *KCNE1* and *KCNE2* are members of the *KCNE* family of genes, and function as ancillary subunits of Kv channels. The third *KCNE* gene, *KCNE3*, is expressed in cardiac myocytes and interacts with KCNQ1 to change the channel properties. However, *KCNE3* has never been linked to LQTS. To investigate the association between *KCNE3* and LQTS, we conducted a genetic screening of *KCNE3* mutations and single nucleotide polymorphisms (SNPs) in 485 Japanese LQTS probands using DHPLC-WAVE system and direct sequencing. Consequently, we identified two *KCNE3* missense mutations, located in the N- and C-terminal domains. The functional effects of these mutations were examined by heterologous expression systems using CHO cells stably expressing KCNQ1. One mutation, p.R99λH was identified in a 76-year-old woman who suffered torsades de pointes (TdP) after administration of disopyramide. Another mutation, p.T4A was identified in a 16-year-old boy and 67-year-old woman. Although the boy carried another *KCNH2* mutation, he was asymptomatic. On the other hand, the woman suffered from hypokalemia-induced TdP. In a series of electrophysiological analyses, the KCNQ1(Q1) +KCNE3(E3)-R99λH channel significantly reduced outward current compared to Q1+E3-WT, though the current density of the Q1+E3-T4A channel displayed no statistical significance. This is the first report of *KCNE3* mutations associated with LQTS. Screening for variants in the *KCNE3* gene is of clinical importance for LQTS patients.

Hum Mutat 30, 557–563, 2009. © 2009 Wiley-Liss, Inc.

KEY WORDS: long QT syndrome; LQTS; *KCNE3*; ion channel; molecular screening; electrophysiology

Introduction

Long QT syndrome (LQTS) is an inherited disease characterized by a prolonged QT interval and a high risk of sudden cardiac death due to peculiar ventricular tachycardia known as torsades de pointes (TdP) [Moss and Kass, 2005]. Most of the LQTS-causing genes encode ion channels, with particular regard to potassium (K) channels. Among them, *KCNE1* (E1) and *KCNE2* (E2) are members of the *KCNE* family (E1 through *KCNE5*) encoding a single-transmembrane-domain proteins. They are called MinK-related peptides (MiRPs) that function as ancillary subunits of Kv channels. In 1999, the third *KCNE* gene, *KCNE3* (ONIM *604433) (E3), was cloned by homology to E1 [Abbott et al., 1999]. In the functional analysis on the KCNQ1 (Q1) +E3 channel, E3 was shown to markedly change Q1 channel properties to yield those activating nearly instantaneously and linearly on voltage [Schroeder et al., 2000].

The expression of E3 in heart was examined and confirmed by northern blot analysis [Schroeder et al., 2000], real-time quantitative RT-PCR [Bendahhou et al., 2005; Lundquist et al., 2005, 2006] and in situ hybridization [Lundquist et al., 2005]. E3 was expressed in all regions of the human heart including left and right ventricles [Lundquist et al., 2005]. The expression level of E3 was larger than that of E2 in every region of the human heart, although smaller than that of E1 [Bendahhou et al., 2005; Lundquist et al., 2005, 2006]. Recently, E3 was reported to

S.O. and F.T. contributed equally to this work.

*Correspondence to: Minoru Horie, M.D., Ph.D., Department of Cardiovascular and Respiratory Medicine, Shiga University of Medical Science, Seta Tsukinowa-cho, Otsu, Shiga, Japan 520-2192. E-mail: horie@belle.shiga-med.ac.jp

Contract grant sponsor: Japan Society for the Promotion of Science; Contract grant sponsor: Ministry of Health, Labour and Welfare, Japan; Grant number: H18-Research on Human Genome-002.

© 2009 WILEY-LISS, INC.

establish a complex with Q1 along with E1 [Morin and Kobertz, 2007]. The Q1+E1+E3 complex generated the current with the combined properties of homomeric Q1+E1 and Q1+E3 complexes, as we previously reported the properties of Q1+E1+E2 complexes [Toyoda et al., 2006]. Taken together, the dysfunction of the Q1+E3 channel may reduce repolarizing K currents in the myocardium, which thereby prolongs the QT interval, although Q1–E3 channels have not yet been demonstrated in the heart.

Abbott et al. [2001] demonstrated a missense mutation of E3 (p.R83λH) in the patients of periodic paralysis. The reduced current densities of the E3-R83λH plus Kv3.4 complex channel in the skeletal muscle caused periodic paralysis, though the authors did not mention cardiac symptoms. More recently, Lundby et al. [2008] identified an E3 mutation (p.V17λM) from an early-onset lone atrial fibrillation (AF) patients. They performed functional analysis of E3-V17λM in coexpression with five kinds of potassium channels. As a result, they revealed increased activity of KV4.3+E3-V17λM and KCNH2+E3-V17λM channels.

During the genetic screening on 485 Japanese LQTS probands, we identified two novel E3 mutations and one reported single nucleotide polymorphism (SNP) (rs34604640:C>G; p.P39R). The mutations were p.T4A in the N-terminal and p.R99λH in the C-terminal. In the present study, we describe the clinical phenotypes of E3-related LQTS patients and the electrophysiological effects caused by these E3 mutations, and assess the probability of E3 as a candidate gene for LQTS.

Materials and Methods

Subjects

Study patients are comprised of 485 congenital and acquired LQTS probands showing prolongation of the QT interval (QTc$\geq$460 ms) or documented TdP from 485 unrelated families. They were referred consecutively to either of our laboratories for genetic evaluation. All subjects submitted written informed consent in accordance with the guidelines approved by each institutional review board. Each underwent detailed clinical and cardiovascular examinations, and were then characterized on the basis of the QT interval in lead V_5 corrected for heart rate (QTc) according to Bazett's formula and the presence of cardiac symptoms.

Genotyping

Genomic DNA was isolated from venous blood lymphocytes as previously described [Ohno et al., 2007]. Through PCR, denaturing high-performance liquid chromatography (DHPLC), and direct DNA sequencing, we performed a comprehensive open reading frame/splice-site mutational analysis of known LQTS genes (*KCNQ1*, *KCNH2*, *SCN5A*, *KCNE1*, and *KCNE2*) using previously described primers [Ohno et al., 2007]. We did not conduct mutational analysis of *ANKB*, *KCNJ2*, *CACNA1C*, *CAV3*, and *SCN4B*. The *KCNE3* coding region was amplified with a primer pair; forward primer; 5′-CTGAGCTTCTACCGAGTCTT-3′ and reverse primer; 5′-TGCAGTCCACAGCAGAGTTC-3′. The size of the PCR product was 435 base pairs. DHPLC analysis of *KCNE3* was performed at three different temperatures; 59.0, 61.2, and 63.5°C. The cDNA sequence was based on GenBank reference sequence NM_005472.4, and the numbering reflects cDNA numbering with +1 corresponding to the A of the ATG translation initiation codon in the reference sequence, according to journal guidelines. The initiation codon is codon 1.

Plasmid Construction

cDNA for human *KCNE3* (NM_005472.4) was cloned into a PCR3.1 plasmid. Variant amino acid residues were constructed using a Quick Change® II XL Site-Directed Mutagenesis Kit (Stratagene, La Jolla, CA), according to the manufacturer's instructions. Nucleotide sequence analysis was performed on each variant construct prior to the expression study.

Construction of a CHO Cell Line Stably Expressing Human KCNQ1

Flp-In CHO cells containing a single integrated Flp recombinase target (FRT) site at a transcriptionally active locus (Invitrogen, Carlsbad, CA) were used for the generation of a stable KCNQ1 cell line. The full-length cDNA fragment of human *KCNQ1* (GenBank AF000571.1) in a pCI vector (a kind gift from Dr. J. Barhanin, Institut de Pharmacologie Moléculaire et Cellulaire, CNRS, Valbonne, France) was subcloned into a pcDNA5/FRT vector (Invitrogen). This construct was cotransfected into Flp-In CHO cells with pOG44, a Flp-recombinase expression vector (Invitrogen), resulting in the targeting interaction of the expression vector. Stable cell clones were selected in hygromycin B (500 μg/ml; Invitrogen), and the expression of KCNQ1 was tested by the whole-cell patch-clamp recording method. One cell line exhibited uniform and homogenous expression of KCNQ1 currents and was used for experiments.

Cell Culture and Transient Transfection

The stable KCNQ1-CHO cell line was maintained in Ham's F-12 medium supplemented with 10% fetal calf serum and 500 &mug/ml hygromycin B in a humidified incubator gassed with 5% CO_2 and 95% air at 37°C. Before transfection, cells were seeded onto 35-mm plastic culture dishes with seven to eight glass coverslips (5λmm × 3λmm) and incubated for 24 to 48λhr. Transient transfection was performed using Lipofectamine (Invitrogen). The amounts of each cDNA used for transfection were (mug/dish): 1.0 *KCNE3*, and 0.5 green fluorescent protein (GFP). At 48 to 72λhr after transfection, only GFP-positive cells were selected for the patch-clamp study.

Patch-Clamp Recordings and Data Analysis

Whole-cell membrane currents were recorded with an EPC-8 patch-clamp amplifier (HEKA, Lambrecht, Germany). A coverslip with adherent CHO cells was placed on the glass bottom of a recording chamber (0.5λml in volume) mounted on the stage of Nikon Diaphot inverted microscope (Tokyo, Japan). Patch pipettes were prepared from glass capillary tube (Narishige, Tokyo, Japan) by means of a Sutter P-97 micropipette puller (Novato, CA), and the tips were then fire-polished with a microforge. Pipette resistance ranged from 2 to 4 Mω when filled with internal solution. Current recordings were conducted at 34±1°C. Voltage-clamp protocols and data acquisition were controlled by PatchMaster software (version 2.03, HEKA) via an LIH-1600 AD/DA interface (HEKA). Cell membrane capacitance (Cm) was measured in every cell by fitting a single exponential function to capacitive transients elicited by 20 ms voltage-clamp steps from a holding potential of −80 mV.

External Tyrode solution contained (mM): 140 NaCl, 0.33 NaH_2PO_4, 5.4 KCl, 1.8 $CaCl_2$, 0.5 $MgCl_2$, 5.4 glucose, and 5 HEPES, and pH was adjusted to 7.4 with NaOH. The internal pipette solution contained (mM): 70 potassium aspartate, 50 KCl, 10 KH_2PO_4, 1 $MgCl_2$, 3 Na_2-ATP, 0.1 Li_2-GTP, 5 EGTA, and 5 HEPES, and pH was adjusted to 7.2 with KOH. Liquid junctional potential between the test solution and the pipette solution was measured to be around −10 mV and was corrected. HMR1556 (a kind gift from Drs. H.J. Lang and J. Pünter, Aventis Pharma Deutschland GmbH) was added from 10 mM stock solution in DMSO to the external solution (final DMSO concentration did not exceed 0.01%).

To obtain the deactivation time constant, the time course of decaying tail current at −50 mV were fitted to a single exponential function:

$$I(t) = A + B\exp(-t/\tau),$$

where I(t) means the tail current amplitude at time t, A and B are constants, and τ is the deactivation time constant.

All data are presented as mean ± standard error of the mean (SEM). Statistical analysis was performed by analysis of variance (ANOVA) followed by Tukey-Kramer post hoc comparison. Statistical significance was set at $P < 0.05$.

Cell Preparation and Confocal Imaging

For the immunofluorescence study, we constructed a hemagglutinin (HA)-tagged *KCNE3* plasmid (wild type [WT] and mutant). An HA epitope (YPYDVPDYA) was introduced into the N-terminus of *KCNE3* cDNA, using an HA-tagged 5′ primer with a KpnI restriction site at the 5′ end and a 3′ primer with BsrGI at the 3′ end. The full-length cDNA fragment of human *KCNQ1* was subcloned into pCI-neo. COS7 cells were transfected with 1.0 &mug of HA-tagged pCR3.1-*KCNE3* (WT or mutant) and 1.0 &mug of pCI-neo-*KCNQ1* plasmid in 35-mm glass-bottom dishes, using Fugene6 (Roche Diagnostics, Basel, Switzerland) according to the manufacturer's instructions. At 48λhr later, the cells were washed twice with phosphate buffered saline (PBS), followed by incubation with a mouse anti-HA primary antibody (1:500) (Covance Research Products, Inc., Berkeley, CA) for 30λminutes at 37°C. The cells were then washed twice with PBS and incubated with an anti-mouse antibody conjugated to the Alexa 488 fluorophore (1:500) (Molecular Probes, Eugene, OR) as a secondary antibody for 30λminutes at 37°C. Finally, cells were washed with and immersed in Opti-Mem, and confocal images were obtained with a Zeiss LSM 510 (Carl Zeiss GmbH, Jena, Germany).

Results

Mutation Analysis

In 485 LQTS probands, we identified two novel missense mutations and one SNP in E3 (Figs. 1 and 2). The first mutation was a single nucleotide alternation (c.296G > A) (Fig. 1A) resulting in an amino acid substitution from an arginine at residue 99 with a histidine (p.R99λH). The second mutation was a single nucleotide change (c.10A > G) (Fig. 2A), causing an amino acid substitution p.T4A, replacing a threonine at residue 4 with an alanine. This T4A missense mutation was identified in two probands. Another proband was found to have a p.P39R polymorphism, which was reported as an SNP (rs34604640: C > G). These three variants were absent in 200 unrelated healthy individuals (400 alleles) from the general Japanese population. They are located in the N-terminus (T4A and P39R) and C-terminus (R99λH), respectively. We further searched for another mutation in LQTS-related genes in these probands carrying E3 mutations (see Materials and Methods). In one of the KCNE3-T4A carriers, we identified a *KCNH2*-p.G572S mutation and in the proband with the P39R polymorphism a *KCNH2*-p.W563G mutation. SNP c.198 T > C (rs2270676), which causes no amino acid substitution (p.F66F), was identified heterozygously in roughly 20% of both LQTS probands and healthy individuals.

Phenotypic Characterization

Patient 1

The novel mutation p.R99λH was found in a 76-year-old female suffering from drug-induced TdP. Her resting 12-lead electrocardiograph (ECG) before administration of disopyramide (Fig. 1B-a) displayed sinus rhythm with normal QTc (438 ms). Because of repeated paroxysmal AF, she was started on 300λmg of disopyramide per day. At 10 days after disopyramide intake, her level of consciousness decreased and ECGs displayed frequent premature ventricular contractions (PVCs) and TdP (Fig. 1B-b). Her heart rate was 66 beats per minute (bpm), and her QTc time was prolonged to 580 ms. Serum K level was within normal range (4.0 mEq/L). Disopyramide was immediately stopped, and temporary pacing was immediately started at 90 bpm. In 3 days, TdP attacks ceased and QTc intervals returned within normal range. She had no family history of sudden cardiac death and LQTS. We did not conduct genetic analyses on the relatives of this patient, due to a lack of consent.

Patient 2

A p.T4A mutation was identified in a 16-year-old boy who had QT prolongation discovered during his school's annual health checkup. He had no history of faintness or syncope and no family history of syncope or sudden death. His resting ECG (Fig. 2B) revealed bradycardia for age (48 bpm) and QT prolongation (QTc = 525 ms). Genetic analysis on other LQTS-related genes revealed a *KCNH2*-G572S missense mutation which had been previously reported [Tester et al., 2005]. His mother and sister also remained asymptomatic but had the same heterozygous set of genetic variants (E3-T4A and *KCNH2*-G572S). Their ECGs also displayed the prolongation of QTc intervals: 520 ms and 560 ms (data not shown).

Patient 3

A p.T4A mutation was also identified in another unrelated proband, a 68-year-old female, who experienced hypokalemia-induced TdP at age 60 years. After correction of serum potassium levels, her QTc time was normalized to 430 msec (Fig. 2C). Two years after the TdP event, she was diagnosed with cardiac sarcoidosis and was started on steroid hormone therapy. Though her daughter also carried the E3-T4A mutation, she was asymptomatic with borderline QTc.

Patient 4

A p.P39R amino acid substitution was identified in a 32-year-old female who was also identified to have a novel *KCNH2* missense mutation, p.W563G. She experienced repeated episodes of late night syncope at ages 15, 21, and 26 years. Figure 3 displays her 12-lead ECG demonstrating marked QT prolongation (QTc = 512 msec) and notched T waves, suggesting LQTS type

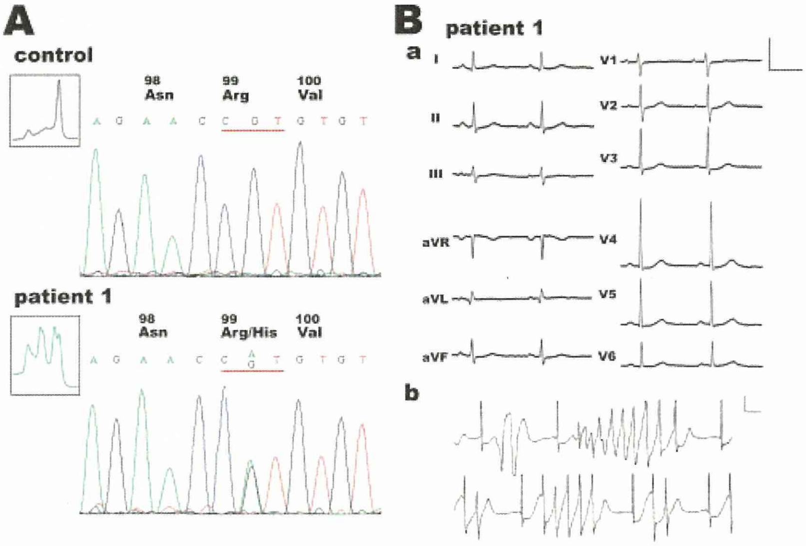

Figure 1. Molecular discovery and clinical characterization of R99H-KCNE3. **A:** DHPLC (insets) and DNA sequence analyses of normal control and Patient 1. DNA sequencing chromatograms demonstrate an arginine (Arg) to histidine (His) substitution at residue 99. **B:** ECGs of Patient 1. (a) 12-lead ECG and (b) monitoring ECG of TdP in a 76-year-old female patient. Scale bars indicate 1 mV and 400 ms. [Color figure can be viewed in the online issue, which is available at www.interscience.wiley.com.]

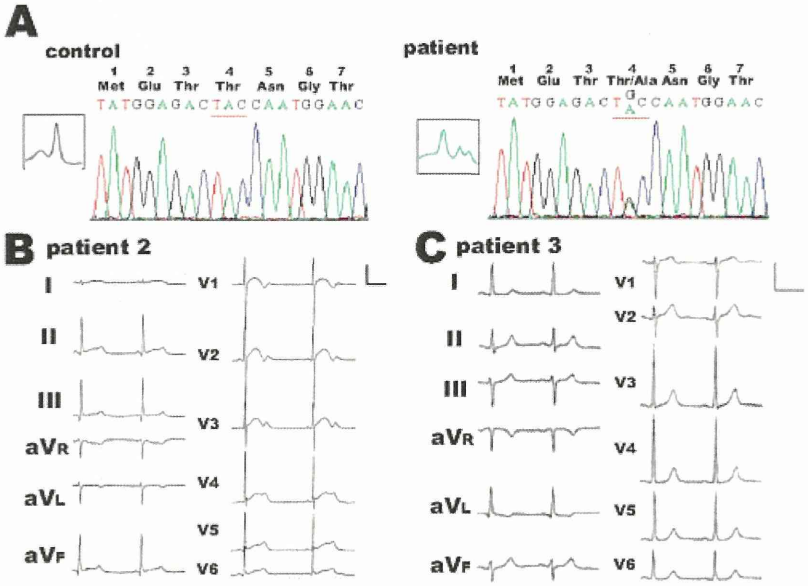

Figure 2. Molecular discovery and clinical characterization of T4A-KCNE3. **A:** DHPLC (insets) and DNA sequence analysis of normal control and patient. DNA sequencing chromatograms demonstrate a threonine (Thr) to alanine (Ala) substitution at residue 4. **B:** The 12-lead ECG of Patient 2. **C:** The 12-lead ECG of Patient 3. [Color figure can be viewed in the online issue, which is available at www.interscience.wiley.com.]

2. E3-P39R was reported as an SNP (rs34604640: C>G); however, P39R was absent in 400 control alleles from healthy Japanese cohorts. Therefore, we conducted a functional analysis of three mutants including P39R.

Biophysical Properties of KCNQ1 Channels Coexpressed With KCNE3

To clarify the functional consequences of these missense mutations (R99λH, T4A, and P39R) on E3, we assessed the biophysical properties of the mutated E3 clone by using the stably expressing human KCNQ1-CHO cell line. Figure 4A shows representative examples of whole-cell currents recorded from CHO cells stably expressing the Q1 channel transfected with or without E3 (WT or mutant). Insets to the right of each recording illustrate expanded views of the tail current elicited after return to –50 mV from test potentials. The current amplitudes were normalized by cell capacitances (current densities). Recordings from cells expressing the Q1 channel alone (left panel of Fig. 4A) displayed small amplitudes of time-dependent outward currents during depolarizing test potentials, followed by slowly deactivating tail currents on return to –50 mV. In contrast, transfection of stable Q1 cells with E3-WT (second panel in Fig. 4A) gave rise to large amplitudes of currents composed of at least two components: 1) a time-dependent outward current activated during depolarizing steps; and 2) a constitutively active background current during depolarizing and hyperpolarizing (–50 mV) steps, as previously reported [Bendahhou et al., 2005; Schroeder et al., 2000]. After the recordings of Q1 with or without E3 current, we applied HMR1556 (1 &muM), a selective Q1 channel blocker. Though the sensitivity on the Q1 alone and Q1+E3 channel of chromanol 293B, another Q1 channel blocker, was different [Bett et al., 2006], both Q1 and Q1+E3 currents were almost totally abolished by only 1 &muM HMR1556 (lower panels of Fig. 4A).

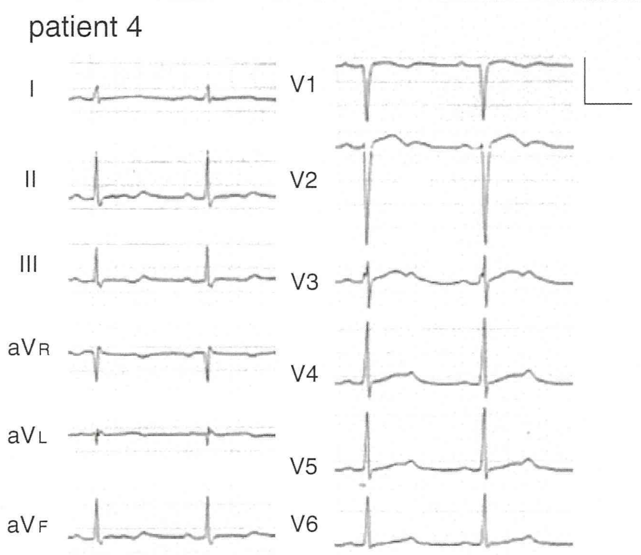

Figure 3. The 12-lead ECG of Patient 4 with QT prolongation. The patient was found to have a KCNE3-SNP, P39R, and a KCNH2-mutation, W536G.

HMR1556-sensitive current densities at the end of test pulse (Fig. 4B) were averaged from data and are plotted as the function of test voltage of Q1 (closed square), Q1+E3-WT (closed circle), Q1+E3-R99λH (open triangle), Q1+E3-T4A (open circle), and Q1+E3-P39R (closed triangle). Currents reconstituted by Q1 alone were activated at potentials greater than –40 mV, whereas those by Q1+E3 (WT and all mutants) were active at all test potentials and exhibited a strong outward rectification with a reversal potential close to E_K (–84 mV as predicted by Nernst equation). All three E3 mutants, E3-R99λH, E3-T4A, and E3-P39R, produced membrane currents with properties qualitatively similar to those of E3-WT. As summarized in Figure 4C, the current densities for the Q1+E3-R99λH current at +40 and –120 mV were 163.7±26.3 and –10.1±2.6 pA/pF, respectively. These values were significantly smaller than those of the Q1+E3-WT (301.6±33.3 pA/pF at +40 mV and –24.5±4.2 pA/pF at –120 mV, $P<0.05$). Q1+E3-T4A and Q1+E3-P39R displayed no statistically significant difference. The deactivation time constant for tail currents was significantly decreased by coexpression of E3 with Q1, but these three mutations in E3 had no significant effect on deactivation kinetics (Fig. 4D).

Cellular Immunocytochemistry of KCNE3

It was reported that no E3 could be expressed on the plasma membrane in the absence of Q1 [Schroeder et al., 2000]. This was reconfirmed in our experimental protocol; the two left columns in Figure 5 show that HA-tagged E3 is not detected by Alexa 488 conjugated HA antibodies in nonpermeabilized COS7 cells in the

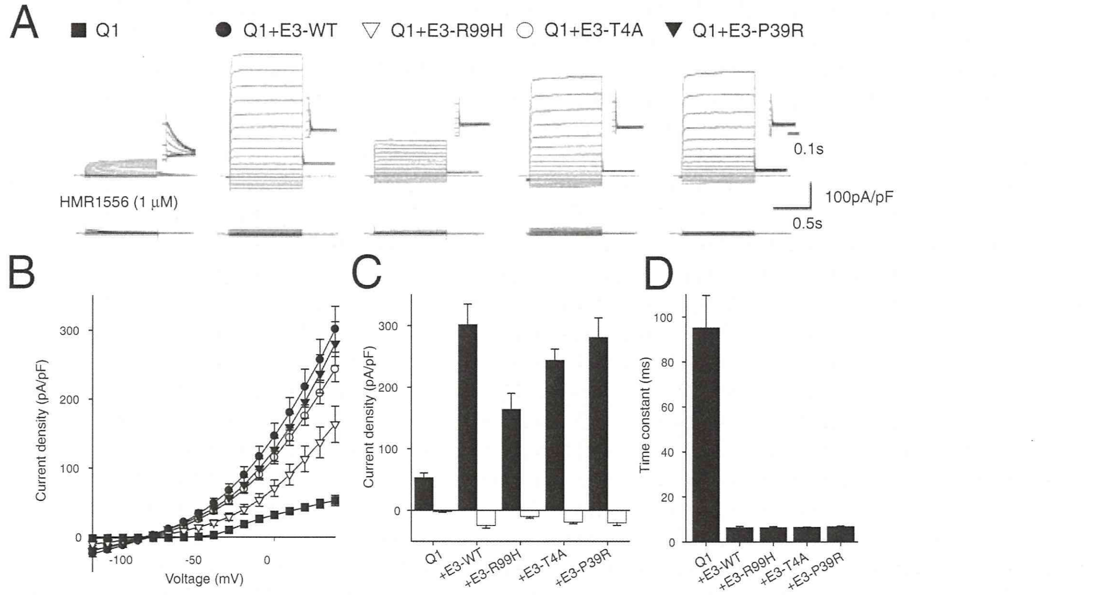

Figure 4. Functional analysis of KCNE3 and its mutants in a CHO cell line stably expressing KCNQ1 channel. **A:** Whole-cell membrane currents recorded from stable KCNQ1-CHO cells transfected without (Q1) or with KCNE3-wild type (Q1+E3-WT), KCNE3-R99λH (Q1+E3-R99λH), KCNE3-T4A (Q1+E3-T4A), or KCNE3-P39R (Q1+E3-P39R). Cells were held at –80 mV and stepped to various test potentials ranging from –120 to +40 mV in 10 mV steps for 1 sec before (upper panel) and during (lower panel) exposure to HMR1556 (1 µM). Dotted line indicates zero current level. Scale bars indicate 0.5 sec and 100 pA/pF. Insets to right of each recording illustrate expanded views of tail current elicited after return to –50 mV from test potentials. Scale bar indicates 0.1 sec. **B:** Current-voltage relationships for mean values of HMR1556-sensitive currents measured at the end of test pulses in CHO cells expressing Q1 (closed square, n = 5), Q1+E3-WT (closed circle, n = 14), Q1+E3-R99λH (open triangle, n = 12), Q1+E3-T4A (open circle, n = 12), or Q1+E3-P39R (closed triangle, n = 10). **C:** Summary of the current density measured at +40 (black bar) and –120 mV (white bar). Columns and error bars indicate mean±SEM. **D:** Deactivation time constant calculated by fitting a single exponential function to tail current at –50 mV after depolarization to +40 mV.

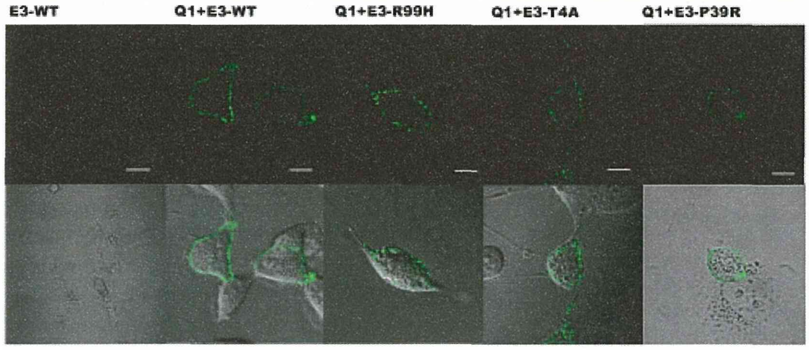

Figure 5. Cell surface expression of WT and mutant KCNE3 channels in nonpermeabilized cell. Upper panels of each column indicate HA-tagged KCNE3 (E3) (WT and three variants) with Alexa 488-conjugated antibodies with or without KCNQ1. Lower panels show merge of green fluorescence and light transmission images. Scale bars indicate 50&mum in E3-WT and 10&mum in others.

absence of Q1 cotransfection. In contrast, HA-tagged E3 could be visualized in the presence of Q1, which indicates that the Q1 protein is necessary for E3 to be successfully trafficked to the cell membrane. Q1 plus HA-tagged E3 channels generated currents similar to those of Q1 plus untagged E3 channels (data not shown). Figure 5 illustrates representative sets of confocal images. COS7 cells were transfected with tagged E3 (WT, T4A, and R99λH) and Q1. All Q1 plus HA-tagged E3 exhibited green fluorescence in the plasma membrane indicating that these channels were trafficked to the plasma membrane normally.

Discussion

In the present study, we report three E3 variants found in 485 LQTS probands. One of the two novel mutations, R99λH, displayed a significant decrease in outward currents when coexpressed with Q1. The proband with the E3-R99λH mutation suffered from drug-induced TdP. After washout of disopyramide, her QTc time on the ECG returned within normal range. The drug probably induced remarkable QT prolongation and TdP in the presence of a reduced repolarization reserve [Roden, 1998], which was associated with the E3-R99λH mutation.

The expression of E3 was confirmed in the human heart [Bendahhou et al., 2005; Lundquist et al., 2005, 2006]. Though neither the presence nor potential function of Q1+E3 channels in human cardiac myocytes have been determined, E3 conformed a functional channel in interaction with Q1, constitutively open potassium channel [Schroeder et al., 2000]. In addition, azimilide-sensitive Q1+E3 like currents were recorded in canine myocytes [Dun and Boyden, 2005]. On account of these results, E3 is assumed to have a physiological role in human heart. Mazhari et al. [2002] studied the effects of E3 on action potential duration (APD) in in vivo transduction of guinea pig ventricular myocytes. APD of E3-transduced myocytes was significantly reduced compared to that of control myocytes. Under the assumption that E3 might interact with KCNH2, they also performed a series of tests using an I_{Kr} blocker (E-4031) to determine whether the APD shortening was due to the interaction with E3 and KCNH2. However, E-4031 did not affect the APD in E3-transduced myocytes. As a result, the APD shortening appeared to be a result of the interaction between Q1 and E3. Although ventricular myocytes are repolarized mainly by Q1+E1 (I_{Ks}) and KCNH2 (I_{Kr}) in human hearts, we believe that the mutant E3 could prolong APD through interaction with Q1. We recently reported the knockdown of E3 expression using RNA interference in guinea pig ventricular myocytes [Toyoda et al., 2008]. The knockdown of E3 was found to prolong the APD, suggesting that E3 may play a physiological role in repolarization of cardiac action potential.

The interaction between KCNH2 and E3 is not established yet. In the experiments using *Xenopus* oocytes, KCNH2 currents were suppressed by coinjection with E3 [Schroeder et al., 2000]. On the contrary, the interaction in horse hearts could not be displayed by means of sequential immunoprecipitation and immunoblotting [Finley et al., 2002]. In addition, the I_{Kr} blocker did not affect APD in E3-transduced myocytes in guinea pigs [Mazhari et al., 2002]. Consequently, we supposed that KCNH2 plus E3 channel would affect very little for repolarization. We therefore did not pursue further examination on the interaction with KCNH2 and E3 using mammalian cell lines.

Regarding the E3-T4A mutation, we postulated that the E3-T4A has minor effects on the QT prolongation, based on the fact that no E3-T4A variant was found in our normal control. Though one of the probands had a *KCNH2*-G572S mutation [Tester et al., 2005] which is supposed to be the major reason for the QT prolongation, another proband had no mutation in major LQTS-related genes. In our biophysical assay, the mutant caused no significant difference in Q1+E3-T4A channel currents; therefore we could not display the association between E3-T4A mutation and QT prolongation. In patient 3, hypokalemia triggered the TdP, accordingly reducing extracellular potassium level may affect the currents through Q1+E3-T4A channels. Or E3 may also interact with another potassium channel alpha-subunit that affects the repolarization of cardiac myocytes, and the E3-T4A mutation may decrease the outward current to prolong QT time. We have to take into account that E3-T4A is a rare SNP, because the correlation between phenotype and genotype in our patients was not common and the number of our control was smaller compared to the studied cases.

E3-P39R may also have functional effects on repolarization. However, our proband with E3-P39R had a compound *KCNH2*-W563G mutation, as well as typical symptoms and ECG findings (Fig. 3) compatible with type 2 LQTS. In addition, functional analysis of the Q1+E3-P39R channel displayed smaller current densities than those of the Q1+E3-WT channel; however there was no statistical difference. Therefore we considered E3-P39R as a rare normal variant in Japanese.

Concerning another α subunit which interacts with KCNE3, Kv4.3 potassium channel encoded by *KCND3* produces transient outward potassium conductance (I_{to}) in the heart and KCNE3 inhibits the Kv4.3 currents [Lundby and Olesen, 2006; Radicke et al., 2006], even in the presence of KChIP2. Hence, there is a possibility that our E3 mutants affect the Kv4.3 current and prolong QT interval.

In conclusion, we identified three E3 variants among 485 Japanese LQTS probands, and one of which significantly reduced currents by interacting with Q1. Though the proband had remained asymptomatic in the absence of risk predisposing to QT prolongation, she fell into highly critical condition by taking disopyramide for AF at age of 76. Therefore, identification of E3 mutations with possible phenotypic effects provides us with information for our understanding of the mechanism of LQTS.

Acknowledgments

We thank the Japanese LQT families for their willingness to participate in this study. We are grateful to Ms. Arisa Ikeda for providing expert technical assistance, and we thank Dr. Takahiro Mitsueda for phenotypic data collection and Mr. Richard Kaszynski for reading the manuscript. W.S., Y.M., and M.H. were supported by a Health Sciences Research grant (H18-Research on Human Genome-002) from the Ministry of Health, Labour and Welfare, Japan.

References

Abbott GW, Sesti F, Splawski I, Buck ME, Lehmann MH, Timothy KW, Keating MT, Goldstein SA. 1999. MiRP1 forms I_{Kr} potassium channels with HERG and is associated with cardiac arrhythmia. Cell 97:175–187.

Abbott GW, Butler MH, Bendahhou S, Dalakas MC, Ptacek LJ, Goldstein SA. 2001. MiRP2 forms potassium channels in skeletal muscle with Kv3.4 and is associated with periodic paralysis. Cell 104:217–231.

Bendahhou S, Marionneau C, Haurogne K, Larroque MM, Derand R, Szuts V, Escande D, Demolombe S, Barhanin J. 2005. In vitro molecular interactions and distribution of KCNE family with KCNQ1 in the human heart. Cardiovasc Res 67:529–538.

Bett GC, Morales MJ, Beahm DL, Duffey ME, Rasmusson RL. 2006. Ancillary subunits and stimulation frequency determine the potency of chromanol 293B block of the KCNQ1 potassium channel. J Physiol 576(Pt 3):755–767.

Dun W, Boyden PA. 2005. Diverse phenotypes of outward currents in cells that have survived in the 5-day-infarcted heart. Am J Physiol Heart Circ Physiol 289:H667–H673.

Finley MR, Li Y, Hua F, Lillich J, Mitchell KE, Ganta S, Gilmour RF, Jr, Freeman LC. 2002. Expression and coassociation of ERG1, KCNQ1, and KCNE1 potassium channel proteins in horse heart. Am J Physiol Heart Circ Physiol 283:H126–H138.

Lundby A, Olesen SP. 2006. KCNE3 is an inhibitory subunit of the Kv4.3 potassium channel. Biochem Biophys Res Commun 346:958–967.

Lundby A, Ravn LS, Svendsen JH, Hauns S, Olesen SP, Schmitt N. 2008. KCNE3 mutation V17λM identified in a patient with lone atrial fibrillation. Cell Physiol Biochem 21:47–54.

Lundquist AL, Manderfield LJ, Vanoye CG, Rogers CS, Donahue BS, Chang PA, Drinkwater DC, Murray KT, George AL, Jr. 2005. Expression of multiple KCNE genes in human heart may enable variable modulation of I_{Ks}. J Mol Cell Cardiol 38:277–287.

Lundquist AL, Turner CL, Ballester LY, George AL, Jr. 2006. Expression and transcriptional control of human KCNE genes. Genomics 87:119–128.

Mazhari R, Nuss HB, Armoundas AA, Winslow RL, Marban E. 2002. Ectopic expression of KCNE3 accelerates cardiac repolarization and abbreviates the QT interval. J Clin Invest 109:1083–1090.

Morin TJ, Kobertz WR. 2007. A derivatized scorpion toxin reveals the functional output of heteromeric KCNQ1-KCNE K^+ channel complexes. ACS Chem Biol 2:469–473.

Moss AJ, Kass RS. 2005. Long QT syndrome: from channels to cardiac arrhythmias. J Clin Invest 115:2018–2024.

Ohno S, Zankov DP, Yoshida H, Tsuji K, Makiyama T, Itoh H, Akao M, Hancox JC, Kita T, Horie M. 2007. N- and C-terminal KCNE1 mutations cause distinct phenotypes of long QT syndrome. Heart Rhythm 4:332–340.

Radicke S, Cotella D, Graf EM, Banse U, Jost N, Varro A, Tseng GN, Ravens U, Wettwer E. 2006. Functional modulation of the transient outward current Ito by KCNE beta-subunits and regional distribution in human non-failing and failing hearts. Cardiovasc Res 71:695–703.

Roden DM. 1998. Taking the "idio" out of "idiosyncratic": predicting torsades de pointes. Pacing Clin Electrophysiol 21:1029–1034.

Schroeder BC, Waldegger S, Fehr S, Bleich M, Warth R, Greger R, Jentsch TJ. 2000. A constitutively open potassium channel formed by KCNQ1 and KCNE3. Nature 403:196–199.

Tester DJ, Will ML, Haglund CM, Ackerman MJ. 2005. Compendium of cardiac channel mutations in 541 consecutive unrelated patients referred for long QT syndrome genetic testing. Heart Rhythm 2:507–517.

Toyoda F, Ueyama H, Ding WG, Matsuura H. 2006. Modulation of functional properties of KCNQ1 channel by association of KCNE1 and KCNE2. Biochem Biophys Res Commun 344:814–820.

Toyoda F, Zankov DP, Ding WG, Matsuura H. 2008. Functional regulation of cardiac KCNQ1 potassium channel by association of KCNE3. [Abstract]. 2008 Biophysics Society Meeting Abstracts, February 2–6, 2008. Biophys J 94(Suppl):3025.

Comput Mech
DOI 10.1007/s00466-009-0432-1

ORIGINAL PAPER

Study of efficient homogenization algorithms for nonlinear problems

Approximation of a homogenized tangent stiffness to reduce computational cost

Jun-ichi Okada · Takumi Washio · Toshiaki Hisada

Received: 30 January 2009 / Accepted: 10 October 2009
© The Author(s) 2009. This article is published with open access at Springerlink.com

Abstract A framework for the homogenization of nonlinear problems is discussed with respect to block LU factorization of the micro–macro coupled equation, and based on the relation between the characteristic deformation and the Schur-Complement as the homogenized tangent stiffness. In addition, a couple of approximation methods are introduced to reduce the computational cost, i.e., a simple scheme to reuse the old characteristic deformation and a sophisticated method based on the mode-superposition method developed by our group. Note that these approximation methods satisfy the equilibrium conditions in both scales. Then, using a simplified FE model, the conventional algorithm, a relative algorithm originating from the block LU factorization, and the above-mentioned algorithms with the approximated Schur-Complement are compared and discussed. Finally, a large-scale heart simulation using parallel computation is presented, based on the proposed method.

Keywords Homogenization method · Nonlinear finite element analysis · Schur-Complement · Mode superposition · Parallel computation · Block LU factorization · Heart

List of symbols

$\mathbf{Y}, \mathbf{y}$	Position vector around the deformation in the microstructure
$\mathbf{X}, \mathbf{x}$	Position vector around the deformation in the macrostructure
$\mathbf{u}$	Macroscopic displacement vector
$\{\mathbf{u}\}$	Macroscopic structure nodal displacement vector
$\{\mathbf{u}^e\}$	Macroscopic structure nodal displacement vector per element
$\mathbf{w}$	Periodic component of the microscopic displacement vector
$\{\mathbf{w}\}$	Periodic component of the nodal displacement vectors of all microstructures
$\{\mathbf{w}^Q\}$	Periodic component of the nodal displacement vector of a single microstructure
$\{\mathbf{w}^e\}$	Periodic component of the nodal displacement vector per element
$\mathbf{F}$	The deformation gradient tensor
$\mathbf{Z}$	The displacement gradient tensor
$\mathbf{C}$	The right Cauchy–Green tensor
$\mathbf{E}$	The Green–Lagrange strain tensor
Π	The first Piola–Kirchhoff stress tensor
$\mathbf{I}$	The identity tensor
I_c, II_c, III_c	Principal invariants
J	Determinant $\mathbf{F}$

1 Introduction

The door to petaflop computing has recently opened and meaningful applications for massively parallel computers are being sought. A multi-scale approach to biomechanical problems is consequential in the post-genome era and the homogenization method is going to play a more important role than ever before. The homogenization method is a mathematical modeling technique for efficiently analyzing inhomogeneous material with a periodic microstructure. In

---

J. Okada (✉) · T. Washio · T. Hisada
Graduate School of Frontier Sciences, University of Tokyo,
5-1-5 Kashiwanoha, Kashiwa, Chiba 277-8563, Japan
e-mail: okada@sml.k.u-tokyo.ac.jp

Published online: 31 October 2009

biomaterial, the periodicity hypothesized in the homogenization method is not strictly established. However, Terada et al. [1] have shown that an appropriate equivalent characteristic is obtained in material with an irregular microstructure by assuming a periodic boundary condition. Thus, it is possible to evaluate the effect of each component in the microstructure on the macroscopic behavior, if microstructure modeling is appropriate. The homogenization method for biomaterial was applied to bone by Hollister and Kikuchi [2], while a two-dimensional analysis of engineered tissue cells was conducted by Breuls et al. [3]. In an example using the heart, Krassowska et al. [4] applied the method to an excitation propagation phenomena. To investigate the effect of intracellular structure on heartbeat, the authors have developed the necessary finite element homogenization method, where the heart is the macrostructure and the cardiomyocyte the microstructure. Thus the problem inevitably becomes a large-scale one.

In the homogenization method two scales are introduced, namely, a scale for the unit period, and a scale for the whole material. By solving the governing equations for both scales with coupling, we can obtain the macroscopic characteristic as an equivalent homogeneous body and variable distribution from the microstructure. In the conventional nonlinear homogenization method [5,6], it is first necessary to calculate microscopic equilibrium and then the macroscopic tangential homogenization updates all quadrature points at every Newton–Raphson iteration, resulting in huge computational cost. Even with a high performance computer, the cost is prohibitive for practical large-scale problems. To reduce this computational cost, various techniques have been devised. These include, for example, the construction of a database with the homogenized properties [7], sensitivity analysis [8], Fast Fourier Transforms [9], and so on. In a previous work, we proposed a homogenization method using characteristic deformation mode superposition [10,11]. This is, however, an approximation method and the accuracy depends on the problem. We subsequently proposed a new algorithm that solves the microscopic equilibrium equation alternately with the solution of the mode superposition-based micro–macro coupled equation. In this algorithm, the equilibrium conditions for both the micro and macro structures are satisfied with far less computational cost. This method is applicable to microstructures composed of slightly incompressible and viscoelastic materials [12–15].

Looking at this method from the block LU factorization of the micro–macro coupled equation, we recognize that the Schur-Complement as the homogenized tangent stiffness, is ingeniously approximated with the aid of mode superposition. It is further beneficial to generalize this view, that is, to interpret the framework of the homogenization method with regard to the block LU factorization and investigate how the Schur-Complement can be approximated to reduce the computational cost whilst preserving the accuracy. Accordingly, a couple of approximation methods, i.e., a simple scheme to reuse the old characteristic deformation and the above-mentioned mode-superposition based method, are introduced in this paper. Then a simplified numerical example is solved using both the conventional homogenization algorithm and the algorithm originating from the block LU factorization, and the performance of each is discussed. Finally, a large-scale heart simulation using parallel computation is presented based on the proposed method.

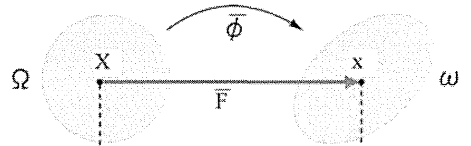

(a) Macro Structure

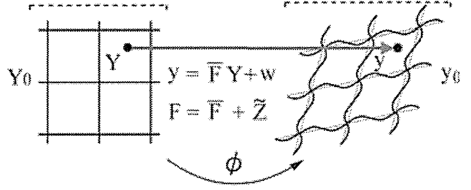

(b) Micro Structure

Fig. 1 Homogenization method for large deformation problems. **a** Macro structure. **b** Micro structure

2 Homogenization method for finite deformation problem

2.1 Problem statement and geometric prospect

We assume that the material in the body (Ω) reveals heterogeneity on a very fine scale and is characterized by the periodic distribution of a basic structural element (Y_0) as shown in Fig. 1. To measure the changes in the spatial domains, we introduce two scales: a macro-scale $X \in \Omega$ and a micro-scale $Y \in Y_0$. Thus the actual domain can be regarded as the product space ($\Omega \times Y_0$). In the subsequent development, the macroscopic quantity corresponding to the microscopic one is expressed with a bar symbol over the microscopic symbol. The following assumptions of homogenization are applied in the formulation of the homogenization method.

- A macrostructure that consists of a periodic microstructure can be considered to be an approximately equivalent homogeneous substance.
- A microstructure is infinitely fine compared with a macrostructure; the variable defined at each point of the macrostructure corresponds to the volume average of the variables in the microstructure.

It is assumed that the deformation of the microstructure is linked to the local values of the macro continuum via

$$\mathbf{y} = \overline{\mathbf{F}}\mathbf{Y} + \mathbf{w}, \tag{1}$$

where $\mathbf{y}$ and $\mathbf{Y}$ are position vectors defined on the microstructure [16].

The deformation consists of a homogeneous part $\overline{\mathbf{F}}\mathbf{Y}$ and a non-homogeneous superposed field $\mathbf{w}$. Consequently, the following relationships exist between the microscopic and macroscopic deformation gradients.

$$\mathbf{F} = \nabla_Y \mathbf{y} = \frac{\partial \mathbf{y}}{\partial \mathbf{Y}} = \overline{\mathbf{F}} + \tilde{\mathbf{Z}}, \tag{2}$$

$$\overline{\mathbf{F}} = \nabla_X \mathbf{x} = \frac{\partial \mathbf{x}}{\partial \mathbf{X}}, \tag{3}$$

$$\tilde{\mathbf{Z}} = \nabla_Y \mathbf{w} = \frac{\partial \mathbf{w}}{\partial \mathbf{Y}}. \tag{4}$$

Thus increment and variation of the deformation gradients are represented, respectively, as

$$\Delta\mathbf{F} = \Delta\overline{\mathbf{F}} + \Delta\tilde{\mathbf{Z}} = \Delta\overline{\mathbf{F}} + \nabla_Y \Delta\mathbf{w}, \tag{5}$$

$$\delta\mathbf{F} = \delta\overline{\mathbf{F}} + \delta\tilde{\mathbf{Z}} = \delta\overline{\mathbf{F}} + \nabla_Y \delta\mathbf{w}. \tag{6}$$

For the assumptions mentioned above, the macroscopic gradients are related via the volume averages

$$\overline{\mathbf{F}} = \frac{1}{|V|}\int\limits_{Y_0} \mathbf{F}dY = \frac{1}{|V|}\int\limits_{Y_0} (\overline{\mathbf{F}} + \tilde{\mathbf{Z}})dY = \overline{\mathbf{F}} + \frac{1}{|V|}\int\limits_{Y_0} \tilde{\mathbf{Z}}dY, \tag{7}$$

where V is the volume of the microstructure Y_0. Then, the fluctuation field $\mathbf{w}$ must satisfy the constraint

$$\int\limits_{Y_0} \tilde{\mathbf{Z}}dY = \int\limits_{Y_0} \frac{\partial \mathbf{w}}{\partial \mathbf{Y}}dY = \int\limits_{\partial Y_0} \mathbf{N} \otimes \mathbf{w}dS = \mathbf{0}, \tag{8}$$

where $\mathbf{N}$ is an outward normal vector on the boundary ∂Y_0. This constraint is satisfied when $\mathbf{w}$ is periodic.

2.2 Formulation of homogenization method and finite element discretization

We now consider the equilibrium of material with a periodic microstructure, modeled by hyperelastic material. Using the principle of stationary potential energy, the equilibrium condition becomes a functional stationary problem. Under the homogenization assumptions, the macroscopic potential energy is related via the volume averages of the microscopic ones and the entire potential energy is defined by

$$\Phi = \int\limits_{\Omega} \frac{1}{|V|}\int\limits_{Y_0} W dY dX - \int\limits_{\partial\Omega} \mathbf{t} \,.\, \mathbf{u} dS, \tag{9}$$

where W is the strain energy function of the microstructure defined by the deformation gradient $\mathbf{F}$, and assuming conservative tractions. The stationary condition becomes

$$\delta\Phi = \int\limits_{\Omega} \frac{1}{|V|}\int\limits_{Y_0} \delta\mathbf{F} : \Pi dY dX - F_{ext}(\delta\mathbf{u}) = 0, \tag{10}$$

$$\Pi = \frac{\partial W}{\partial \mathbf{F}}, \tag{11}$$

$$F_{ext}(\delta\mathbf{u}) = \int\limits_{\partial\Omega} \mathbf{t} \,.\, \delta\mathbf{u} dS. \tag{12}$$

A similar equation has been reported by Terada and Kikuchi [5] using two-scale convergence theory [17]. We have also shown a formulation based on the mixed variational principle with a perturbed Lagrange-multiplier [14]. By inserting Eq. (6) into Eq. (10), macro and micro equilibrium equations can be derived based on the defined space of the variation.

$$\overline{G} = \int\limits_{\Omega} \frac{1}{|V|}\int\limits_{Y_0} \delta\overline{\mathbf{F}} : \Pi dY dX - F_{ext}(\delta\mathbf{u}) = 0, \tag{13}$$

$$G = \int\limits_{Y_0} \delta\tilde{\mathbf{Z}} : \Pi dY = 0, \tag{14}$$

which achieves equilibrium under the given boundary condition in the macrostructure and self-equilibrium under a periodic boundary condition, Eq. (8), of the microscopic displacement in the microstructure. Thus the homogenization method simultaneously satisfies the two equilibrium conditions as described above. To solve the nonlinear equation, the Newton–Raphson method is employed. Then the standard linearization process in nonlinear finite element method provides the following linearized equations

$$\int\limits_{\Omega} \frac{1}{|V|}\int\limits_{Y_0} \delta\mathbf{F} : \mathbf{A} : \Delta\mathbf{F} dY dX = F_{ext}(\delta\mathbf{u}) - \int\limits_{\Omega} \frac{1}{|V|}\int\limits_{Y_0} \delta\mathbf{F} : \Pi dY dX, \tag{15}$$

$$\mathbf{A} = \frac{\partial \Pi}{\partial \mathbf{F}}. \tag{16}$$

Substituting Eqs. (5) and (6) into the above equation yields

$$\int\limits_{\Omega} \frac{1}{|V|}\int\limits_{Y_0} s(\delta\overline{\mathbf{F}} + \delta\tilde{\mathbf{Z}}) : \mathbf{A} : (\Delta\overline{\mathbf{F}} + \Delta\tilde{\mathbf{Z}}) dY dX = F_{ext}(\delta\mathbf{u}) - \int\limits_{\Omega} \frac{1}{|V|}\int\limits_{Y_0} (\delta\overline{\mathbf{F}} + \delta\tilde{\mathbf{Z}}) : \Pi dY dX. \tag{17}$$

By finite element discretization using

$$\Delta\overline{\mathbf{F}} = [\overline{B^e}]\{\Delta\mathbf{u}^e\}, \tag{18}$$

$$\Delta\tilde{\mathbf{Z}} = [B^e]\{\Delta\mathbf{w}^e\}, \tag{19}$$

where $[B^e]$ is a shape function matrix, the left-hand side of Eq. (17) becomes

$$\begin{aligned}
&\{\delta\mathbf{w}^Q\}\frac{1}{|V|}\int_{Y_0}[B^e]^T[A][B^e]dY\{\Delta\mathbf{w}^Q\}\\
&\quad+\{\delta\mathbf{w}^Q\}\frac{1}{|V|}\int_{Y_0}[B^e]^T[A]dY[\overline{B^e}]\{\Delta\mathbf{u}^e\}\\
&\quad+\{\delta\mathbf{u}^e\}[\overline{B^e}]^T\frac{1}{|V|}\int_{Y_0}[A][B^e]dY\{\Delta\mathbf{w}^Q\}\\
&\quad+\{\delta\mathbf{u}^e\}[\overline{B^e}]^T\frac{1}{|V|}\int_{Y_0}[A]dY[\overline{B^e}]\{\Delta\mathbf{u}^e\}\\
&=\{\delta\mathbf{w}^Q\}\mathbf{K}^Q_{ww}\{\Delta\mathbf{w}^Q\}+\{\delta\mathbf{w}^Q\}\mathbf{K}^Q_{wu}\{\Delta\mathbf{u}^e\}\\
&\quad+\{\delta\mathbf{u}^e\}\mathbf{K}^Q_{uw}\{\Delta\mathbf{w}^Q\}+\{\delta\mathbf{u}^e\}\mathbf{K}^Q_{uu}\{\Delta\mathbf{u}^e\},
\end{aligned}\tag{20}$$

while the second term of the right-hand side of Eq. (17) becomes

$$-\{\delta\mathbf{u}^e\}[\overline{B^e}]^T\frac{1}{|V|}\int_{Y_0}[\Pi]dY-\{\delta\mathbf{w}^Q\}\frac{1}{|V|}\int_{Y_0}[B^e]^T[\Pi]dY,\tag{21}$$

at each quadrature point of the macrostructure. Symbol Q denotes the quantity that is evaluated at a macroscopic quadrature point, while symbol e denotes the quantity evaluated in the macroscopic element. By assembling these appropriately on the macro continuum, and considering the facultative variations, the following semi-positive definite symmetric matrix is obtained

$$\begin{bmatrix}\mathbf{K}_{ww} & \mathbf{K}_{wu}\\ \mathbf{K}_{uw} & \mathbf{K}_{uu}\end{bmatrix}\begin{Bmatrix}\Delta\mathbf{w}\\ \Delta\mathbf{u}\end{Bmatrix}=\begin{Bmatrix}\mathbf{r}_w\\ \mathbf{r}_u\end{Bmatrix},\tag{22}$$

where

$$\mathbf{K}_{ww}=\int_{\Omega}\left(\frac{1}{|V|}\int_{Y_0}[B^e]^T[A][B^e]dY\right)dX\tag{23}$$

$$\mathbf{K}_{wu}=\int_{\Omega}\left(\frac{1}{|V|}\int_{Y_0}[B^e]^T[A]dY\right)[\overline{B^e}]dX\tag{24}$$

$$\mathbf{K}_{uw}=\int_{\Omega}[\overline{B^e}]^T\left(\frac{1}{|V|}\int_{Y_0}[A][B^e]dY\right)dX\tag{25}$$

$$\mathbf{K}_{uu}=\int_{\Omega}[\overline{B^e}]^T\left(\frac{1}{|V|}\int_{Y_0}[A]dY\right)[\overline{B^e}]dX\tag{26}$$

$$\{\mathbf{r}_w\}=-\int_{\Omega}\left(\frac{1}{|V|}\int_{Y_0}[B^e]^T[\Pi]dY\right)dX\tag{27}$$

$$\{\mathbf{r}_u\}=F_{ext}-\int_{\Omega}[\overline{B^e}]^T\left(\frac{1}{|V|}\int_{Y_0}[\Pi]dY\right)dX.\tag{28}$$

The nonlinear homogenization method solves Eq. (22) for $\Delta\mathbf{u}$ and $\Delta\mathbf{w}$ under the given boundary condition for the macrostructure and the periodic boundary condition (Eq. 8) for microscopic displacement. The number of degrees of freedom (NDOF) of this matrix is (NDOF of macrostructure + quadrature point of macrostructure × NDOF of microstructure). An enormous computational cost is, however, required to solve a small-scale problem. Moreover, it is difficult to solve the form given in Eq. (8) due to memory limitations, and generally, a transformation into the weak form takes place as described below.

2.3 Characteristic deformation

In a nonlinear problem, to evaluate the response of a microstructure to macroscopic deformation in a similar way to that in a linear problem [18], we obtain the following equation by taking the derivative of Eq. (14) at each quadrature point and substituting Eqs. (5) and (16).

$$\int_{Y_0}\delta\tilde{\mathbf{Z}}:\mathbf{A}:d\tilde{\mathbf{Z}}dY=-\int_{Y_0}\delta\tilde{\mathbf{Z}}:\mathbf{A}:d\overline{\mathbf{F}}dY\tag{29}$$

Since the macroscopic deformation gradient is independent of the microscopic integration,

$$\int_{Y_0}\delta\tilde{\mathbf{Z}}:\mathbf{A}:\frac{\partial\tilde{\mathbf{Z}}}{\partial\overline{\mathbf{F}}}dY=-\int_{Y_0}\delta\tilde{\mathbf{Z}}:\mathbf{A}:\mathbf{I}dY,\tag{30}$$

where $\mathbf{I}$ is a fourth order identity tensor, and the microstructural response of the macroscopic deformation gradient becomes

$$\frac{\partial\tilde{\mathbf{Z}}}{\partial\overline{\mathbf{F}}}=\nabla_Y\left(\frac{\partial\mathbf{w}}{\partial\overline{\mathbf{F}}}\right)\equiv-\nabla_Y\chi,\tag{31}$$

$$\chi\equiv-\frac{\partial\mathbf{w}}{\partial\overline{\mathbf{F}}},\tag{32}$$

where a third order tensor χ is the derivative of the microscopic displacement with respect to the macroscopic deformation gradient. This is referred to as the characteristic deformation for nonlinear problems. The equation above can be substituted into Eq. (30) yielding

$$\int_{Y_0}\delta\tilde{\mathbf{Z}}:\mathbf{A}:\nabla_Y\chi dY=\int_{Y_0}\delta\tilde{\mathbf{Z}}:\mathbf{A}:\mathbf{I}dY.\tag{33}$$

By finite element discretization, the gradient of χ becomes

$$\nabla_Y \chi = [B^e][\chi^e], \tag{34}$$

in a microscopic finite element. $[\chi^e]$ is the derivative of the microscopic displacement for each component of $\overline{\mathbf{F}}$; in other words, it is the matrix given below with nine kinds of characteristic deformation.

$$[\chi^e] = \begin{bmatrix} \chi^e_{111} & \chi^e_{112} & \cdots & \chi^e_{133} \\ \chi^e_{211} & \chi^e_{212} & \cdots & \chi^e_{233} \\ \vdots & \vdots & \ddots & \vdots \\ \chi^e_{n11} & \chi^e_{n12} & \cdots & \chi^e_{n33} \end{bmatrix}, \tag{35}$$

where n is the NDOF of one finite element of the microstructure. The matrix equation becomes

$$\mathbf{K}_\chi [\chi^Q] = [\mathbf{r}_\chi], \tag{36}$$

$$\mathbf{K}_\chi = \int_{Y_0} [B^e]^T [A][B^e] dY, \tag{37}$$

$$[\mathbf{r}_\chi] = \int_{Y_0} [B^e]^T [A][I] dY, \tag{38}$$

from Eq. (33) about one microstructure. $[\chi^Q]$ denotes that the quantity is evaluated at the macroscopic quadrature point. The value of $[\chi^Q]$, which is a (NDOF of the microstructure) row × 9 column matrix, can be obtained by assembling $[\chi^e]$. $[I]$ is a ninth order identity matrix, consisting of nine column vectors $\{I_i\} (i = 1 \ldots 9)$. Thus nine solutions can be obtained for the right-hand side of Eq. (38), one for each $\{I_i\}$ corresponding to a component of the deformation gradient. $[\chi^Q]$ can then be obtained by solving each different version of the right-hand side of the above equation.

Multiplying by $[\overline{B^e}]$ and dividing by $|V|$ on both sides, Eq. (36) yields

$$\frac{1}{|V|} \mathbf{K}_\chi [\chi^Q][\overline{B^e}] = \frac{1}{|V|} [\mathbf{r}_\chi][\overline{B^e}]. \tag{39}$$

Now, by using Eq. (20)

$$\frac{1}{|V|} \mathbf{K}_\chi = \mathbf{K}^Q_{ww}, \tag{40}$$

$$\frac{1}{|V|} [\mathbf{r}_\chi][\overline{B^e}] = \mathbf{K}^Q_{wu}, \tag{41}$$

and thus,

$$\mathbf{K}^Q_{ww} [\chi^Q][\overline{B^e}] = \mathbf{K}^Q_{wu}. \tag{42}$$

The total is obtained at all macroscopic quadrature points in respect of the above equation

$$\mathbf{K}_{ww} [\chi][\overline{B}] = \mathbf{K}_{wu}, \tag{43}$$

$$[\overline{B}] \equiv \sum_i [\overline{B^e}], \tag{44}$$

$$[\chi] \equiv \sum_i [\chi^Q], \tag{45}$$

where $[\chi]$ is a matrix consisting of (quadrature points of macrostructure × NDOF of microstructure) rows × 9 columns.

The characteristic deformations are the deformation increments for unit macroscopic deformation gradients at a particular instant and these describe the material properties and strain distribution of the microstructure. Equation (29) can also be considered a linear approximation of the microscopic deformation. Therefore, the update of the microscopic deformation by

$$\Delta \mathbf{w} = -\chi : \Delta \overline{\mathbf{F}}, \tag{46}$$

corresponds to the Forward Euler method for microscopic deformation from Eq. (32).

2.4 Homogenization method using characteristic deformation mode superposition

In the mode superposition homogenization method, the microscopic displacement increment is approximately obtained by the linear combination of the previously calculated characteristic deformation ${}_0\chi$ and the scaling factor from Eq. (46) as in [10]

$$\Delta w_k \doteqdot -{}_0\chi_{kpQ} \Delta \alpha_{pQ}, \tag{47}$$

where α is the scaling factor for each mode. Inserting Eq. (47) into Eq. (22) yields the matrix

$$\begin{bmatrix} [{}_0\chi]^T & \mathbf{0} \\ \mathbf{0} & \mathbf{I} \end{bmatrix} \begin{bmatrix} \mathbf{K}_{ww} & \mathbf{K}_{wu} \\ \mathbf{K}_{uw} & \mathbf{K}_{uu} \end{bmatrix} \begin{bmatrix} [{}_0\chi] & \mathbf{0} \\ \mathbf{0} & \mathbf{I} \end{bmatrix} \begin{Bmatrix} \Delta\alpha \\ \Delta\mathbf{u} \end{Bmatrix} = \begin{bmatrix} [{}_0\chi]^T & \mathbf{0} \\ \mathbf{0} & \mathbf{I} \end{bmatrix} \begin{Bmatrix} \mathbf{r}_w \\ \mathbf{r}_u \end{Bmatrix} \tag{48}$$

$$\begin{bmatrix} [{}_0\chi]^T \mathbf{K}_{ww} [{}_0\chi] & [{}_0\chi]^T \mathbf{K}_{wu} \\ \mathbf{K}_{uw} [{}_0\chi] & \mathbf{K}_{uu} \end{bmatrix} \begin{Bmatrix} \Delta\alpha \\ \Delta\mathbf{u} \end{Bmatrix} = \begin{Bmatrix} [{}_0\chi]^T \mathbf{r}_w \\ \mathbf{r}_u \end{Bmatrix}, \tag{49}$$

where $[{}_0\chi]$ is the same kind of matrix as $[\chi]$. The above equation can be represented as

$$\begin{bmatrix} \mathbf{K}_{\alpha\alpha} & \mathbf{K}_{\alpha u} \\ \mathbf{K}_{u\alpha} & \mathbf{K}_{uu} \end{bmatrix} \begin{Bmatrix} \Delta\alpha \\ \Delta\mathbf{u} \end{Bmatrix} = \begin{Bmatrix} \mathbf{r}_\alpha \\ \mathbf{r}_u \end{Bmatrix}, \tag{50}$$